

Renata Latypova

DEVELOPMENT AND
APPLICATION OF A NOVEL
TUNING-FORK TEST IN
STUDYING HYDROGEN-
INDUCED FRACTURE IN AS-
QUENCHED MARTENSITIC
STEELS

UNIVERSITY OF OULU GRADUATE SCHOOL;
UNIVERSITY OF OULU,
FACULTY OF TECHNOLOGY



ACTA UNIVERSITATIS OULUENSIS
C Technica 856

RENATA LATYPOVA

**DEVELOPMENT AND APPLICATION
OF A NOVEL TUNING-FORK TEST IN
STUDYING HYDROGEN-INDUCED
FRACTURE IN AS-QUENCHED
MARTENSITIC STEELS**

Academic dissertation to be presented with the assent of the Doctoral Programme Committee of Technology and Natural Sciences of the University of Oulu for public defence in the Arina auditorium (TA105), Linnanmaa, on 9 December 2022, at 12 noon

UNIVERSITY OF OULU, OULU 2022

Copyright © 2022
Acta Univ. Oul. C 856, 2022

Supervised by
Professor Jukka Kömi
Doctor Saara Mehtonen
Doctor Sakari Pallaspuuro

Reviewed by
Professor Kim Verbeken
Docent Rachel Pettersson

Opponents
Research Professor Elina Huttunen-Saarivirta
Docent Rachel Pettersson

ISBN 978-952-62-3509-7 (Paperback)
ISBN 978-952-62-3510-3 (PDF)

ISSN 0355-3213 (Printed)
ISSN 1796-2226 (Online)

Cover Design
Raimo Ahonen

PUNAMUSTA
TAMPERE 2022

Latypova, Renata, Development and application of a novel tuning-fork test in studying hydrogen-induced fracture in as-quenched martensitic steels.

University of Oulu Graduate School; University of Oulu, Faculty of Technology

Acta Univ. Oul. C 856, 2022

University of Oulu, P.O. Box 8000, FI-90014 University of Oulu, Finland

Abstract

Hydrogen embrittlement (HE) is a well-recognized issue with ultrahigh-strength steels (UHSS) and an intensively studied subject to minimize the risk of sudden, catastrophic failures in structural applications. A novel tuning-fork test (TFT) is developed in this thesis to study HE of UHSS. The testing method utilizes constant displacement for stressing of the tuning-fork specimens by bending, combined with electrochemical hydrogen charging. With an isolated tensile stress region, crack initiation is controlled and can be monitored with different clamping arrangements. The main objectives were to create a simple and fast testing method, which allows ranking of UHSS, and to investigate the effects of prior austenite grain (PAG) structure. Traditional hydrogen permeation tests with a set-up built within this thesis complement the results.

The first part of the TFT implementation is composed of an evaluation of the HE susceptibility of 300–600 HBW martensitic steels with relative threshold stress levels. Increasing the strength level leads to lower threshold stress levels and increased susceptibility to HE, especially for steels with over 400 HBW hardness. With the addition of a loadcell to the TFT clamping system, a more precise investigation was conducted for 500 HBW steels with various PAG structures. The effect of PAG morphology (elongated/equiaxed) on HE susceptibility was studied with steels that had different alloying compositions and with steels that had different PAG morphologies but the same alloying.

An elongated PAG structure leads to enhanced resistance against HE in comparison to equiaxed PAG structures. Crack propagation rates were slower with more elongated microstructure, which is linked to transgranular quasi-cleavage crack propagation and slower hydrogen diffusion. Equiaxed microstructure exhibits partly intergranular cracking with faster crack propagation rate and hydrogen diffusion. Crack propagation was affected by the microstructure alignment of the elongated PAG structure, but the equiaxed structure did not show orientation differences. No correlation was observed between hydrogen diffusivities and different PAG boundary surface areas. However, the density of reversible hydrogen traps increased with decreasing amount of PAG boundaries, indicating that PAG boundaries may act as strong hydrogen traps in the investigated steels.

Keywords: diffusion, hardness, hydrogen, hydrogen embrittlement, martensite, prior austenite grain structure, steel, strength

Latypova, Renata, Uuden äänirautakokeen kehittäminen ja soveltaminen karkaistujen martensiittisten terästen vetyhauraustutkimuksessa.

Oulun yliopiston tutkijakoulu; Oulun yliopisto, Teknillinen tiedekunta

Acta Univ. Oul. C 856, 2022

Oulun yliopisto, PL 8000, 90014 Oulun yliopisto

Tiivistelmä

Ultralujien terästen vetyhauraus on tunnettu ilmiö, jonka tutkiminen on tärkeää koska se voi pahimmillaan johtaa äkkinäisiin, rakenteiden katastrofaalisiin vaurioihin. Tässä työssä kehitetään uutta testausmenetelmää nimeltään äänirautakoe (Tuning-Fork Test, TFT) ultralujien terästen vetyhaurauden tutkimiseksi. Äänirautakokeessa yhdistetään vakiosiiirtymän kautta määritetty elastinen jännitystila ja sähkökemiallinen vetylataus. Erityyppisten geometrioiden ja puristimien avulla äänirautanäytteeseen vaikuttava jännitystila saatiin rajattua tarkasti alueelle, jossa särön ydintyminen tapahtuu, jolloin särönkasvua voidaan kontrolloida ja seurata. Väitöskirjan päättävöitteena oli kehittää nopea ja yksinkertainen testausmenetelmä, joka mahdollistaa ultralujien terästen vertailun ja mikrorakenteellisten tekijöiden vaikutuksen tutkimisen vedyn aiheuttamassa murtumisessa. Täydentävää tutkimusta tehtiin perinteisellä vedyn permeaatiokokeella.

Ensimmäisessä vaiheessa 300–600 HBW kovuusluokan martensiittisten terästen taipumusta vetyhaurauteen arvioitiin määrittämällä terästen suhteellinen kynnysjännitys. Tulokset osoittavat kovuuden/lujuuden kasvun lisäävän teräksen alttiutta vetyhaurauteen, joka korostuu teräksen kovuuden ollessa yli 400 HBW. Voima-anturin lisääminen testauslaitteistoon paransi mittaustarkkuutta, ja mahdollisti perinnäisen austeniitin raerakenteen vaikutuksen tutkimisen. Vertailussa käytettiin 500 HBW teräksiä, jotka erosivat perinnäisen austeniitin muodon (venynyt/tasa-aksiaalinen) ja koon suhteen ja osa seostukseltaan.

Venynyt perinnäisen austeniitin raerakenne paransi vetyhaurauden kestoa. Särön etenemisnopeus oli hitaampi venyneessä mikrorakenteessa, joka johtui rakeiden läpi etenevästä murtumasta sekä hitaammasta vedyn diffuusiosta. Tasa-aksiaalisessa rakenteessa vedyn diffuusio oli nopeampaa ja särön etenemisnopeus kasvoi ja murtuma tapahtui osittain raerajamurtumana. Mikrorakenteellinen anisotropia vaikutti särön etenemiseen venyneissä rakeissa. Tasa-aksiaalisessa mikrorakenteessa ei havaittu suuntautuneisuuseroja. Vedyn diffuusion ja perinnäisen austeniitin raerajapinta-alan välillä ei havaittu korrelaatiota. Kun perinnäisen austeniitin raerajoja oli vähemmän, heikkojen vetyloukkujen tilavuus kasvoi, mikä viittaa siihen, että perinnäisen austeniitin raerajat toimivat vahvoina vetyloukkuina tutkituissa teräksissä.

Asiasanat: diffuusio, kovuus, lujuus, martensiitti, perinnäisen austeniitin raekoko, teräs, vety, vetyhauraus

To my beloved family and friends

Acknowledgements

The research for this thesis was performed at the Materials and Mechanical Engineering unit at the University of Oulu, Finland, from 2018 to 2022. It was funded by the Business Finland projects “Steel Ecosystem for Focused Applications” (StEFA), “Intelligent Steel Applications” (ISA), “Fossil-Free Steel Applications” (FOSSA), and the Academy of Finland project “Materials Performance Competence Spearhead” (PerForMat). Financial assistance in the form of personal grants by the Jenny and Wihuri Foundation, Walter Ahlström Foundation, and Tauno Tönning Foundation is acknowledged. The materials for this research were provided by SSAB Europe Oy.

I wish to express my gratitude to my thesis supervisors Prof. Jukka Kömi, Dr. Sakari Pallaspuro, and Dr. Saara Mehtonen for their continuous guidance and support during this work. I would also like to thank my thesis advisor Prof. Emeritus Hannu Hänninen for his invaluable help and encouragement throughout my thesis. My doctoral committee including Dr. Anna Kisko, Dr. Olli Nousiainen, and Prof. Jari Larkiola are thanked for their valuable contributions.

To all my colleagues at the Materials and Mechanical Engineering unit, thank you. Many of you have provided important assistance to my research, which is highly appreciated: Dr. Antti Kaijalainen, M.Sc. Oskari Seppälä, M.Sc. Sami Koskenniska, Dr. Oskari Haiko, and M.Sc. Sampo Uusikallio. Special thanks go to Lic.Sc. Timo Kauppi who has always believed in me and provided necessary advice as a teacher, master’s thesis supervisor, and finally as a colleague. Furthermore, the efforts of Mr. Ilpo Saarela, M.Sc. Kasper Hahtonen, and all workshop staff are appreciated, especially the work of Mr. Kaarlo Vähätaini with the loadcell clamp. A big thank you to M.Sc. Tun Tun Nyo whose input in experimental work in the laboratory was irreplaceable.

Finally, I would like to thank my family and friends for their sincere encouragement and unconditional support during these years.

Oulu, December 2022

Renata Latypova

List of abbreviations, definitions and symbols

A	surface area difference
AIDE	adsorption-induced dislocation emission
BCC	body-centred cubic
BCT	body-centred tetragonal
C	carbon
CE	counter electrode
CERT	constant extension rate test
CL	constant load
CO ₂	carbon dioxide
CPR	crack propagation rate ($\mu\text{m/s}$)
D	diffusion coefficient (cm^2/s)
DQ	direct quenching
DS	Devanathan-Stachurski
e.g.	exempli gratia; for example
EBSD	electron backscatter diffraction
EP	electrochemical permeation
FCC	face-centred cubic
FEM	finite element method
FESEM	field-emission scanning electron microscope
FRT	finish rolling temperature
GUI	graphical user interface
H	hydrogen
HBW	Brinell hardness
HE	hydrogen embrittlement
HEDE	H enhanced decohesion
HELP	H enhanced localized plasticity
HESIV	hydrogen-enhanced strain-induced vacancies
HISCC	hydrogen-induced stress corrosion cracking
HMT	hydrogen microprint technique
i.e.	id est; that is
LIST	linearly increasing stress test
LTT	low-temperature tempering
MMO	mixed metal oxide
ND	normal direction
PAG	prior austenite grain

QT	quenching and tempering
RD	rolling direction
RE	reference electrode
RQ	reheated and quenched
RQT	reheated, quenched, and tempered
SCC	stress corrosion cracking
SSRT	slow strain rate test
TDS	thermal desorption spectroscopy
TFT	tuning-fork test
TS	tensile strength (MPa)
UHSS	ultrahigh-strength steels
WE	working electrode
WEDM	wire electrode discharge machining
wt.%	weight fraction in percent
C_H	subsurface hydrogen concentration (mol/m ³)
d_G	prior austenite grain size (μm)
ϵ	epsilon carbide
M_s	martensite start temperature (°C)
N_T	reversible hydrogen trap density (sites/cm ³)
R_m	tensile strength (MPa)
S_V	grain boundary surface area (mm ² /mm ³)
t_f	time to fracture (min)
t_i	initiation time (min)
t_p	propagation time (min)
η	eta carbide
σ_{th}	threshold stress (MPa)
σ_{th}/R_m	relative threshold stress

List of original publications

This thesis is based on the following publications, which are referred throughout the text by their Roman numerals:

- I Latypova, R., Kauppi, T., Mehtonen, S., Hänninen, H., Porter, D., & Kömi, J. (2019). Novel stress corrosion testing method for high-strength steels. *Materials and Corrosion*, 70(3), 521–528. doi:10.1002/maco.201810462
- II Latypova, R., Nyo, T. T., Kauppi, T., Pallaspuro, S., Mehtonen, S., Hänninen, H., & Kömi, J. (2020). Hydrogen-induced stress corrosion cracking studied by the novel tuning-fork test method. *Materials and Corrosion*, 71(10), 1629–1636. doi:10.1002/maco.202011767
- III Latypova, R., Seppälä, O., Nyo, T. T., Kauppi, T., Pallaspuro, S., Mehtonen, S., Hänninen, H., Kömi, J. (2020). Hydrogen-induced cracking of 500 HBW steels studied using a novel tuning-fork test with integrated loadcell system. *Corrosion*, 76(10), 954–966. doi:10.5006/3592
- IV Latypova, R., Seppälä, O., Nyo, T. T., Kauppi, T., Mehtonen, S., Hänninen, H., Kömi, J., Pallaspuro, S., Influence of prior austenite grain structure on hydrogen-induced fracture of as-quenched martensitic steels, submitted manuscript.

Publication I and II focus on the preliminary development of the novel tuning-fork test with the ranking and categorization of 300 – 600 HBW ultrahigh-strength steels by their hydrogen embrittlement susceptibility. In Publication III, the tuning-fork test is drastically improved by the integration of a loadcell system, which allows for monitoring different crack propagation stages. The influence of prior austenite grain morphology in the hydrogen-induced fracture is studied with three different 500 HBW steels using the tuning-fork test with an integrated loadcell system. However, different manufacturing routes and alloying complicate the comparison between the PAG morphologies. Therefore, in the last publication, Publication IV, the tuning-fork tests, as well as the traditional hydrogen permeation tests, are conducted with three materials with the same alloying composition, similar mechanical properties, but different prior austenite grain morphologies. Same alloying allows the thorough investigation of the effect of prior austenite grain shape and size on hydrogen-induced fractures.

The author of this dissertation is the main and corresponding author in all the listed publications. She prepared the research plan, conducted literature reviews, produced the laboratory-made materials, designed the experiments, and wrote the manuscripts. She also conducted materials characterization and fractography. Furthermore, she was in charge of the technical development of the tuning-fork test, which includes the cell, cover, clamp, and specimen geometry designs that are

presented in this thesis. The permeation cells, including glass cells, clamping, and sealing system were also designed by the main author. The data was analysed and interpreted together with the co-authors.

The roles of co-authors besides result analysis and reviewing the manuscript are the following: Tun Tun Nyo has been closely involved in test method development, experimental work, and specimen preparation for all Publications, finite element modelling was provided by Oskari Seppälä throughout the thesis with graphical analysis tools for Publications III – IV, and Sakari Pallaspuro provided the necessary assistance with fractographic work and EBSD measurements.

Contents

Abstract	
Tiivistelmä	
Acknowledgements	9
List of abbreviations, definitions and symbols	11
List of original publications	13
Contents	15
1 Introduction	17
1.1 Background	17
1.2 Aims of the research	18
2 Theoretical foundation	21
2.1 Martensitic ultrahigh-strength steels	21
2.1.1 Prior austenite grain structure.....	24
2.2 Hydrogen embrittlement in high-strength steels	25
2.2.1 H-induced fracture.....	27
2.2.2 Testing methods.....	29
3 Experimental	31
3.1 Experimental materials	31
3.2 Experimental methods.....	32
3.2.1 Tuning-fork testing.....	32
3.2.2 Hydrogen permeation tests	39
3.3 Materials characterization	41
4 Results and discussion	43
4.1 Relative threshold stress level.....	43
4.2 Crack propagation phases	47
4.2.1 Unnotched specimens.....	47
4.2.2 Notched specimens.....	52
4.2.3 Interrupted tuning-fork tests	61
4.3 Hydrogen permeation.....	63
5 Summary and conclusions	67
5.1 Tuning-fork testing.....	67
5.2 PAG structure.....	67
6 Novel features	69
7 Future research	71
List of references	73
Original publications	81

1 Introduction

1.1 Background

The essential facts about the deleterious effects of hydrogen (H) on the mechanical properties of steel have been known for over 140 years. The earliest publication regarding HE goes back to 1875 when diffusible hydrogen was proved to be the cause of embrittlement, as well as the fact that stronger steel is more susceptible to hydrogen in comparison to softer versions [1], [2].

HE leads to a degradation of the mechanical properties of steel such as loss of ductility, as well as reduction of strength and toughness due to an interaction with hydrogen. As the smallest atom, hydrogen can readily diffuse inside the material, and at a critical concentration and sufficient tensile stress, cause fracture [3]. The consequences of hydrogen embrittlement can be catastrophic due to the unpredictable nature of the phenomenon. Today, it is widely accepted that higher strength leads to a higher susceptibility to HE in steels, which limits the applicability of high-strength as well as ultrahigh-strength steels in operations with hydrogen.

Ultrahigh-strength steels are one of the most important materials in our modern society. The superior combination of strength, toughness, and formability has led to their broad utilization in various sectors such as structural, automotive, mining, and agricultural industries. One of the main arguments for the utilization of ultrahigh-strength steels are environmental factors. Because of the high strength, it is possible to use less material or thinner wall thickness, leading to energy savings through reduced mass of the steel applications. In vehicles, weight reduction can significantly affect fuel consumption and therefore lower greenhouse gas emissions, such as CO₂, which has a global effect on the environment [4]. The CO₂ emissions can be lowered further by utilizing hydrogen as an alternative energy carrier [5]. However, that will require different transport and storage solutions with equipment that can withstand hydrogen. Ultrahigh-strength steel is a prospective material choice for these structures, but it will also be challenging due to the risk of hydrogen embrittlement (HE).

Many factors, such as microstructure, alloy composition, production route, environment, and applied stress level and state, affect HE susceptibility. Therefore, optimization of microstructure can improve performance of ultrahigh-strength

steels in hydrogen-containing environments, which enables their wider serviceability.

Hydrogen-induced fracture in ultrahigh-strength steels propagates typically along the prior austenite grain (PAG) boundaries, which is called intergranular crack propagation. PAG boundaries can act as diffusion paths or trapping sites for hydrogen, which can cause sudden failures by the separation of these grain boundaries [6]. Therefore, HE susceptibility can be influenced through modifications of PAG structure, such as size, shape, and grain boundary characteristics [7]. This thesis focuses primarily on the PAG structure of ultrahigh-strength steels and its effect on HE susceptibility.

1.2 Aims of the research

The main aim of the research work was to determine how PAG shape and size affect susceptibility to hydrogen embrittlement in different 500 HBW ultrahigh-strength steels. The shape of the PAG structure depends on the steel manufacturing process, mainly the final rolling temperature. PAGs can be elongated/pancaked with irregular shapes or equiaxed with a more symmetrical shape. In both cases, there can be many variations in grain size depending on the alloying and production route of steel. To execute this study, two different test methods are designed and built, which is a major part of this thesis. The objectives of this thesis can be divided as follows:

- Development and verification of a novel tuning-fork testing (TFT) method for fast HE susceptibility ranking of ultrahigh-strength steels.
- Implementation of the TFT for studying hydrogen-induced cracking mechanisms.
- Design, development, and implementation of an electrochemical hydrogen permeation test (EP).
- Establishing the relationship between PAG shape/size and hydrogen embrittlement susceptibility of ultrahigh-strength steels.
- Understanding the effect of PAG structure on the crack propagation mechanism of ultrahigh-strength steels.
- Characterization of hydrogen diffusion and trapping properties mainly depending on the PAG structure.

The listed objectives are addressed in three peer-reviewed journal articles (Publications I – III) and in submitted manuscript (Publication IV). The results from

the articles are summarized and discussed in this thesis with future consideration given in the final chapter. The short outline of the thesis is given in Fig. 1.

	Publication I	Publication II	Publication III	Publication IV
Topic	Test method development			
	Steel ranking		PAG anisotropy	
Test materials (steels)	450, 500, 600 HBW	300, 400, 500 and 550 HBW	3 different 500 HBW (different alloying)	3 different 500 HBW (same alloying)
Testing methods	TFT			EP

Fig. 1. Thesis outline, where TFT = tuning-fork test and EP = electrochemical permeation.

2 Theoretical foundation

2.1 Martensitic ultrahigh-strength steels

There is no universally accepted definition or strength level for ultrahigh-strength steels, but they are described as structural steels that have very high strength levels [8], [9]. Some sources use yield strength and others tensile strength to create an arbitrary limit to separate high- and ultrahigh-strength steels. For example, yield strength can vary up to 1380 MPa and the tensile limits have been reported to be 780 – 1270 MPa [9], [10]. In this study, the lowest tensile strength of materials is 940 MPa, and therefore they will be referred as ultrahigh-strength steels throughout this thesis. The most common type of ultrahigh-strength steels are steels with martensitic microstructure. Martensite has two possible microstructures depending on the carbon content, i.e., plate- or “needle-like” (> 1 wt.% C) and lath-martensite (< 0.6 wt.% C) [3]. This thesis will focus on low-carbon (≤ 0.30 wt.% C) steels with lath-martensitic microstructure.

Martensite is a metastable phase that is known for its high hardness and strength but low ductility. The austenite-martensite phase transformation causes formation of internal stresses and dislocations due to shear and volume expansion, which contribute to the mechanical properties of a steel [3], [11], [12]. The as-quenched martensitic microstructure contains a fraction of untransformed austenite, which is referred to as retained or residual austenite [13]. In low-carbon martensitic microstructure, the retained austenite is present as very thin inter-lath films [14].

Martensite is the strongest of ferrous microstructures, which is formed by quenching from face-centred cubic (FCC) lattice of austenite. During quenching, the transformation from austenite to martensite starts at a certain temperature, which is called the martensite start temperature (M_s) which depends on alloying, especially the carbon content [14]. The transformation is ideally diffusionless, where the austenite-martensite transformation occurs almost instantaneously, while the carbon remains as interstitial atoms in the martensite. However, it is mainly theoretical since the complete suppression of carbon diffusion is virtually impossible and diffusional phase transformation can occur during quenching. For low-carbon martensitic steels, the M_s temperature is usually high and carbon mobility is sufficient to cause fine cementite precipitation during quenching, i.e., auto-tempering [15].

Martensite has typically a body-centred tetragonal (BCT) cubic structure, which is a body-centred cube (BCC) slightly elongated along one of its dimensions. [11] However, low-carbon martensitic steels have essentially near-BCC structure due to carbon segregation to dislocations and auto-tempering [16]. During quenching, the parent austenite grain divides into several structural: laths, blocks, and packets. Laths are single crystals, with approximately 0.2 – 0.5 μm thickness, which are separated by low-angle boundaries with a misorientation angle of less than 5° [3], [17]. The laths with the same orientation are grouped into blocks and blocks are further grouped into packets. Block, packet, and prior austenite grain boundaries are high-angle boundaries with a misorientation angle of at least 15° [18], [19]. All structural units resulting from austenite-martensite transformation are presented in Fig. 2.

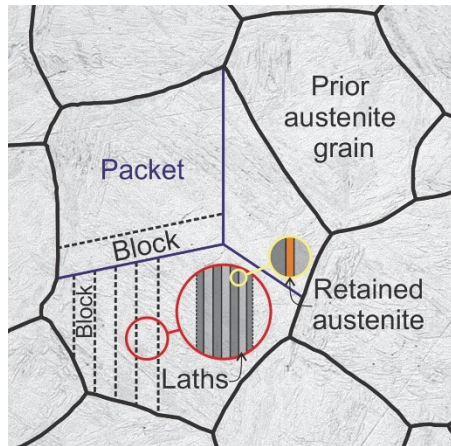


Fig. 2. Schematic of lath-martensitic microstructure.

The traditional way to manufacture martensitic ultrahigh-strength steels is called reheating and quenching (RQ), reheat-quenching and tempering (RQT), or simply quenching and tempering (QT). The process starts with the soaking of slabs, followed by hot rolling of plates and air cooling. After cooling, the plates are cut to the desired size, re-austenitized, and quenched to martensite [4]. Quenching has to be rapid to prevent carbon diffusion and the formation of ferrite and cementite phases [20]. Nevertheless, cementite precipitation may occur due to auto-tempering if the onset temperature of martensite (M_s) is high enough.

The final step in RQT is tempering (150 – 700 $^\circ\text{C}$), which is used to improve the mechanical properties, especially toughness. Various types of tempered

microstructures can be achieved depending on the tempering temperature [14]. For QT steels, low-temperature tempering (LTT) in the range of 100 – 200 °C is often applied. During LTT, martensite experiences partial loss in tetragonality due to carbon diffusion, and transition carbides such as eta (η) and epsilon (ϵ) carbides are formed [12], [14]. However, low-carbon steels do not have apparent tetragonality, and because of auto-tempering, there is no sufficient driving force for formation of transition carbides. Therefore, mainly minor carbon segregation and relief of residual stresses are expected to occur during LTT [16], [21].

A modern way to produce martensitic ultrahigh-strength steels is direct-quenching (DQ) or direct-quenching and tempering (DQT), which are thermomechanical rolling processes integrated with direct-quenching. In this case, no additional reheating and quenching is applied since quenching is done right after slab soaking and controlled rolling. Because of auto-tempering, i.e., tempering during quenching and consecutively improved toughness, separate tempering treatment is not necessary. Without additional reheating, quenching, and tempering, DQ is more cost-efficient in comparison to RQ [4]. Fig. 3 presents the schematic time-temperature diagrams of the traditional RQ production route (a) and DQ (b).

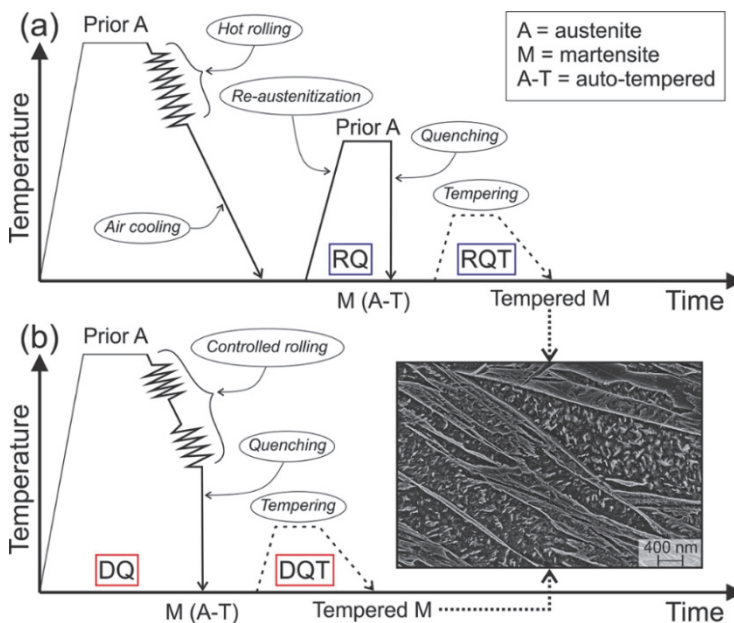


Fig. 3. Schematic of two different production routes of martensitic ultrahigh-strength steels: (a) RQ/RQT, and (b) DQ/DQT.

2.1.1 Prior austenite grain structure

The PAG size and shape are inherited in the martensitic structure affecting its performance and mechanical properties such as strength, toughness, and ductility [12], [20]. In traditionally manufactured RQ steel, austenite is fully recrystallized before quenching, which produces an equiaxed PAG morphology in the final martensitic microstructure. With RQ steels, PAG size is mainly controlled by the austenitization temperature.

In contrast, quenching of DQ steel happens immediately after hot rolling where austenite is either in recrystallized, partially recrystallized, or non-recrystallized form depending on the temperature and steel composition. If this thermomechanical treatment is conducted below recrystallization finish temperature, martensite formation will occur from deformed, unrecrystallized austenite. The final PAG structure will then have an elongated/pancaked morphology in the rolling direction [4]. The degree of pancaking is affected by the finish rolling temperature (FRT), where a lower temperature leads to a higher elongation [22]. Elongated PAG structure can be also achieved by ausforming or tempforming treatments, which utilize deformation at even lower temperatures in comparison to the DQ process [7], [23].

The level of elongation of the PAG structure is usually expressed as the RD/ND grain size ratio, where RD is the rolling direction and ND is the normal direction of the steel plate. Fig. 4a presents an example of elongated PAG structure with a RD/ND ratio of 3 and Fig. 4b an equiaxed PAG structure with a ratio of 1.

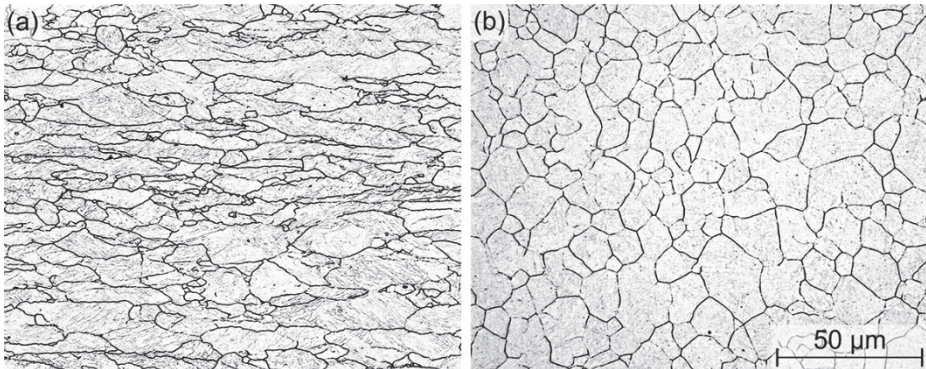


Fig. 4. PAG structures: (a) elongated/pancaked, and (b) equiaxed.

Because of the suppressed recrystallization, the PAG substructure of DQ steels has a high degree of crystallographic discontinuities, which act as potential nucleation sites for martensite. Therefore, formation of martensite from deformed austenite (DQ) leads to a finer grain size in the martensitic microstructure in comparison to deformation-free austenite (RQ) [24], [25].

2.2 Hydrogen embrittlement in high-strength steels

Hydrogen embrittlement of high-strength steels is unwanted brittleness in metals that is caused by the presence of hydrogen inside the material [26]. Martensitic steels are especially prone to HE due to their high strength, but susceptibility is also affected by alloy composition, production route, residual stresses, surface condition, and the applied stress level and state. Another significant factor is the environment, which comprises pressure, temperature, exposure time, and amount of hydrogen [27]. HE is also the predominant mechanism in hydrogen-induced stress corrosion cracking (HISCC) of high-strength steels [26], [28].

Hydrogen is the lightest element in the periodic table, and its natural state is a diatomic molecular gas (H_2). Molecular hydrogen is too large to cross the surface of solid metal or to diffuse interstitially inside the metal. Therefore, entry and diffusion of H require dissociation of the hydrogen molecule into its nascent/monoatomic form (H) [3], [29]. Hydrogen uptake can occur in various stages of manufacturing or service, which divides HE into internal or external depending on the source of hydrogen. Internal HE refers to hydrogen uptake during manufacturing process, i.e., embrittlement occurs with the application of load as a result of inherited or pre-existing hydrogen in the steel [30]. In external HE, hydrogen is introduced to the material surface from, e.g., gaseous or aqueous environments during service [31]. In HISCC, hydrogen forms from cathodic corrosion reactions. For example, in the mining industry, sulphuric acid lowers mine water pH and causes an accelerating breakdown of minerals by the corrosion reactions that produce hydrogen [32].

After entering the steel, hydrogen diffusion and trapping take place. Hydrogen diffusion is a concentration gradient-driven process, with hydrogen diffusing towards the regions of triaxial tensile stresses. HE occurs after reaching a certain critical concentration. The diffusion of hydrogen happens interstitially or along dislocations or grain boundaries, but the diffusion rate is hindered if H gets trapped by various microstructural features inside the material [3], [33], [34]. Dislocations are important hydrogen traps, and their mobility can be enhanced or reduced by

different hydrogen-dislocation interactions. Hydrogen diffusion can be accelerated by moving dislocations with trapped hydrogen or by short-range pipe diffusion [3], [35]. Grain boundaries can also interact with hydrogen in two different ways, as hydrogen traps and as fast conduit for hydrogen diffusion [3]. There are many other possible trapping sites depending on the given microstructure, such as vacancies, solutes, precipitates, inclusions, interfaces, and voids. Especially martensitic steels have many interfaces, such as lath, block, packet, and PAG boundaries, which attract hydrogen. Depending on the trap binding energy, traps can be divided into reversible and irreversible trapping sites, which can be beneficial or detrimental in terms of HE. Irreversible traps have high binding energy, and hydrogen becomes immobile or non-diffusible. With a finite amount of hydrogen and well-distributed irreversible traps, HE sensitivity can be reduced. On the other hand, reversible traps can hold and release hydrogen, which can subsequently diffuse to highly stressed lattice sites. Therefore, reversible trapped hydrogen and diffusible hydrogen are considered to induce HE [2], [36]. Fig. 5 presents the possible weak and strong trapping sites in steel.

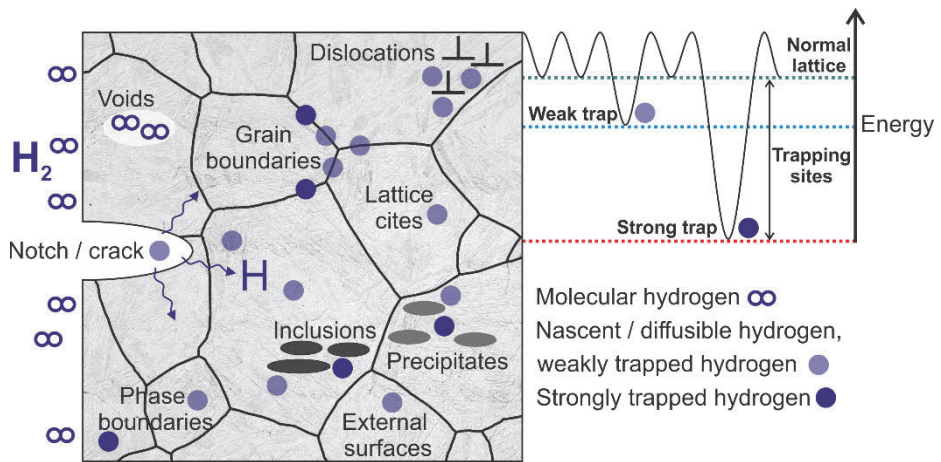


Fig. 5. Examples of hydrogen traps in steel.

Several mechanisms are used to describe HE, such as H Enhanced DEcohesion (HEDE), H Enhanced Localized Plasticity (HELP), hydrogen-enhanced-plasticity mediated decohesion, Adsorption-Induced Dislocation Emission (AIDE) and hydrogen-enhanced strain-induced vacancies (HESIV). HEDE is based on the weakening/decohesion of interatomic bonds of metal in the presence of a critical

amount of H, which causes brittle crack propagation under tensile loads. Intergranular crack propagation can be explained by HEDE, with a high amount of hydrogen accumulating at grain boundaries and with a high enough concentration causing fracture. According to the HELP mechanism, hydrogen enhances the dislocation motion, resulting in localized plastic deformation and accelerated failure. In hydrogen-enhanced-plasticity mediated decohesion, HELP and HEDE act simultaneously, and cracking mechanisms are distinguished by the location of the dislocations pile-ups. Intergranular cracking takes place if dislocation pile-up impinge PAG boundaries and quasi-cleavage when dislocation pile-ups impinge on block boundaries causing the already weakened boundaries to debond by the pile-up stresses [38]. AIDE is a combination of HEDE and HELP since it involves the weakening of atomic bonds and dislocation movement at regions of stress concentrations with microvoid growth at the crack tip [34], [39]. HESIV mechanism proposes that hydrogen accelerates the formation of strain-induced vacancies and their agglomeration which facilitates void initiation, growth, and occurrence of premature fracture [40]. The research is still ongoing and none of the mentioned major mechanisms are yet fully accepted [27], [39], [41]. However, the combination of different mechanisms is currently gaining acceptance [35].

2.2.1 H-induced fracture

There are no specific fracture types for hydrogen embrittlement, and a range of hydrogen degradation mechanisms can be observed in different microstructures. Generally, two fracture types are possible in metals: ductile fracture with dimpled fracture surface and brittle fracture, which has intergranular, transgranular cleavage, or transgranular quasi-cleavage features. Ductile fracture manifests plastic deformation with high energy absorption before fracture, while brittle fracture occurs suddenly and catastrophically without significant prior plastic deformation [11], [29].

Intergranular fracture propagates primarily along PAG boundaries, and transgranular fracture through grains. In case of intergranular fracture, fracture surfaces exhibit three-dimensional grains with exposed grain boundary surface facets, which are produced by decohesion of the PAG boundaries. In transgranular cleavage, atomic bonds are ruptured, which causes the separation of the specific crystalline planes or “cleavage planes”. The separated facets have a smooth and shiny appearance [11], [42], [43]. Quasi-cleavage is also transgranular, but it does not follow the typical cleavage planes. It is described with facet morphologies that

are not as planar as cleavage facets, but have complex, non-uniform features such as river markings, serrated marking, step lines, and tear ridges [44]. Examples of ductile fracture with dimples and brittle fracture with intergranular, transgranular cleavage and transgranular quasi-cleavage fracture surfaces are presented in Fig. 6.

In lath-martensitic steels, HE-caused fractures usually involve brittle intergranular fractures along PAGs or quasi-cleavage fracture mechanisms [45]. Resistance to HE can be improved by modifying the PAG structure (e.g., size, shape, grain boundary characteristics) so that the intergranular crack propagation is suppressed [7], [46]. This thesis will concentrate on how PAG size and morphology affect the hydrogen embrittlement of ultrahigh-strength steels.

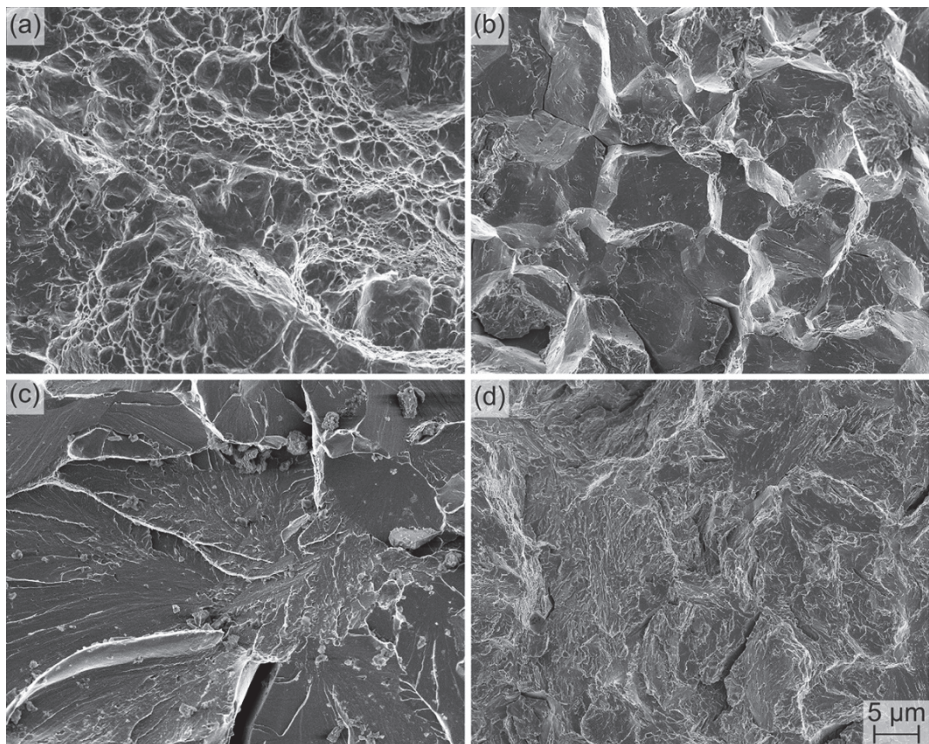


Fig. 6. Examples of (a) ductile, (b) brittle intergranular, (c) transgranular cleavage, and (d) transgranular quasi-cleavage fracture surfaces of steels.

2.2.2 Testing methods

There are many available testing methods for studying the hydrogen embrittlement of steel. Most of them utilize mechanical loading with tensile test equipment, e.g., constant load tests (CL), constant extension rate test (CERT)/slow strain rate test (SSRT), and linearly increasing stress test (LIST) combined with hydrogen charging. Typically, smooth/notched specimens are subjected to fracture tests in hydrogen charged/uncharged conditions and hydrogen effect on, e.g., time of failure, yield strength, tensile strength, elongation, reduction in area, and fracture morphology are investigated. In the CL test, specimens are under a static load, while in CERT/SSRT, constantly increasing elongation is applied, and LIST is a load-controlled testing method [3], [27], [31], [47].

The easiest way to introduce H atoms inside the material is by electrochemical hydrogen charging, although gaseous and plasma charging can be utilized [48], [49]. Usually, the charging electrolyte is selected so that it mimics the real-life operating environment of the investigated material. For example, diluted sulphuric acid can be used to study abrasive resistant steels, which simulates their service environment encountered in the mining industry.

Often, so-called hydrogen poisons such as thiourea ($\text{CH}_4\text{N}_2\text{S}$), ammonium thiocyanate (NH_4SCN), and arsenic trioxide (As_2O_3) are added to the electrolyte to inhibit H_2 recombination and therefore accelerate the hydrogen uptake during charging [50]–[52]. There are two techniques for hydrogen charging: galvanostatic and potentiostatic. In galvanostatic hydrogen charging, a constant current density is applied, and in potentiostatic hydrogen charging, constant potential is applied while the specimen acts as a cathode. Galvanostatic hydrogen charging is easier since it requires only a test specimen acting as the working electrode (WE) and a counter electrode (CE) acting as the anode. In potentiostatic hydrogen charging, a three-electrode set-up is required with WE, CE, and a reference electrode (RE). Apart from mechanical testing, there are other methods for studying hydrogen in steel, such as thermal desorption spectroscopy (TDS), electrochemical permeation test, the Ag decoration method, and hydrogen microprint technique (HMT). TDS is useful in quantifying the hydrogen trap strength by determining the activation energy. Hydrogen permeation is used for studying the diffusivity, permeability, and trapping properties of steel, and Ag decoration/HMT can visualize hydrogen ingress and egress sites in steel [3], [27], [31].

3 Experimental

3.1 Experimental materials

For this work, a variety of direct-quenched steel grades with nominal hardness levels of 300 – 600 HBW as well as one RQ steel with 500 HBW hardness were provided by the steel manufacturer SSAB Europe. All delivered materials are 6 mm thick, hot-rolled strip products with essentially martensitic microstructure. The nominal hardness, production route, chemical compositions (in wt.%), and associated Publication of the used materials are summarized in Table 1. Tensile test and hardness test results of all steel grades were provided by the steel manufacturer.

Table 1. Nominal hardness, production route, and chemical composition (in wt.%) of all steel grades studied in this thesis. Different 500 HBW steels are numbered 1 – 3 in subscript.

Steel (HBW)	Production route	C	Mn	Si	S	Publication
300	DQ	0.087				II
400	DQ	0.145				II
450	DQ	0.216	1.30	0.17		I
500 ₁	DQ	0.264	1.14	0.21	0.003	I, III
500 ₂	DQ	0.251	0.25		0.002	II – IV
Re-austenitized at 860 °C + quenched	DQ + RQ		0.25			IV
Re-austenitized at 960 °C+ quenched	DQ + RQ		0.25			IV
500 ₃	RQ	0.240	0.68		0.001	III
550	DQ	0.336				II
600	DQ	0.364	0.37	0.21		I

Experimentally, this thesis divides into two parts. The first part is test method development and verification, where materials are investigated in the as-delivered state (Publications I – III). The second part is the implementation of the novel testing method in investigations of the effects of PAG structure of differently manufactured ultrahigh-strength steels on their susceptibility to HE (Publications III – IV).

For Publication IV, laboratory-scale austenitization and quenching were conducted with 500₂ steel which has an elongated PAG morphology. Steel plates (300x250x6 mm) were first austenitized at 860/960 °C with a 20 min holding time and subsequently quenched into water-oil emulsion to create different-sized, equiaxed PAG structures with the same alloying composition. In addition to

ultrahigh-strength steels, a commercial Armco iron is utilized as the reference material in hydrogen permeation experiments in Publication IV.

3.2 Experimental methods

3.2.1 Tuning-fork testing

The tuning-fork test was used at different stages of its development throughout all Publications. It is a unique constant-displacement test, which can be used to study hydrogen-induced fracture of high-strength steels. The tuning-fork test provides information regarding the material-specific threshold stress, but also about initiation time, time-to-fracture, propagation time, and crack propagation rate. After the tests, fracture surfaces can be studied to understand crack propagation mechanisms.

The original work with the tuning-fork test was started in 2016 by Alexander Chernyaev, who published the results in a master's thesis titled "Development of a rapid stress corrosion cracking test method for high-strength steels" [53]. This work was continued in my own master's thesis, and test method development proceeded further in this dissertation. The results from my master's thesis are presented in Publication I, where the testing method was officially named a tuning-fork test because of the specimen geometry.

The motivation for the TFT test method development was to create a simple and fast test that can be used for ranking of ultrahigh-strength steels by their hydrogen-induced stress corrosion cracking (HISCC) susceptibility. The goal was to combine a restricted tensile stress region with a hydrogen-containing corrosive environment. Along the way, the test method underwent many changes in test specimens, clamping, cells, environment, and charging conditions, and turned into a hydrogen embrittlement test. However, all test versions had the same main principles as follows:

1. Calculation of stress levels by finite element method (FEM) models for each material
2. Clamping of the specimen
3. Hydrogen charging of the specimen until fracture

During the test method development, one objective was not to use tensile test equipment, which is usually necessary for the traditional CERT/SSRT or CL tests

in HE studies. Specimen selection was also challenging because utilization of traditional geometries such as bent-beam [54], [55], C-ring [56], U-bend [57], [58], and self-loaded tensile specimens [59] was considered complicated due to the high strength of the test materials. Specimen modifications are usually difficult to perform identically in order to avoid the unwanted spring back, overloading, distortion, misalignment, and stress relaxation with time. All the above-mentioned reasons led to the selection of the “tuning-fork” specimens. The design was based on the tuning-fork geometry, which has been utilized earlier in SCC testing of aluminium alloys [60].

All tuning-fork specimens were produced by wire-electrode discharge machining (WEDM) from 150x50x5 mm plates. Before WEDM, 0.5 mm/side was machined from the plates to achieve the 5 mm specimen thickness. WEDM causes microstructural changes on the cut surfaces, and an approximately 4 μm softer layer forms due to the elevated temperature during cutting as presented in Fig. 7. To eliminate any WEDM-caused microstructural discontinuities, outer specimen surfaces were polished before the testing.

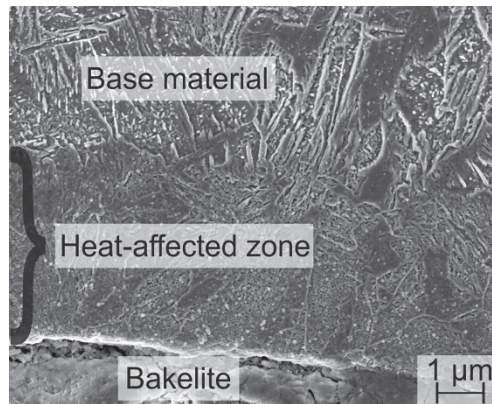


Fig. 7. WEDM affected zone at the cut specimen surface. (Reprinted, with permission, from Publication IV © 2022 Authors).

The tuning-fork geometries which were used for this thesis are presented in Fig. 8. There are only small changes in the geometries, such as the leg difference between geometry 1 and 2, which was made to improve the clamping and polishing of the specimens. The last and final geometry 3 has an additional notch at the narrower part of the specimen arm to ensure a specific tensile stress concentration.

Apart from specimen geometry, specimen orientation was considered as well. Two-letter and one-letter codes were used to name specimen orientation, L-T or shortened L and T-L or shortened T. The first letter refers to the direction of normal to the crack plane, and the second letter designates the expected direction of crack propagation as presented in Fig. 9.

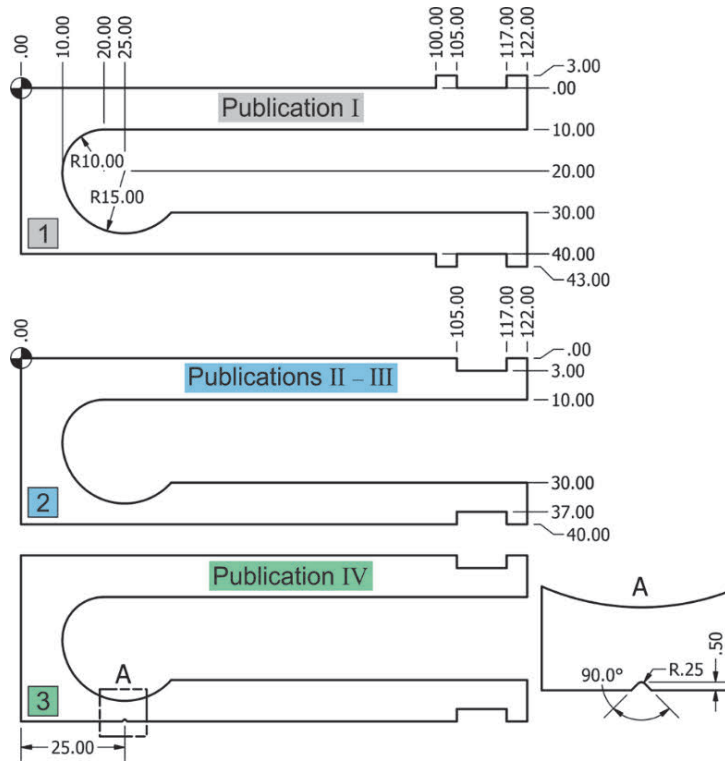


Fig. 8. The evolution of tuning-fork specimen geometry in Publications I – IV.

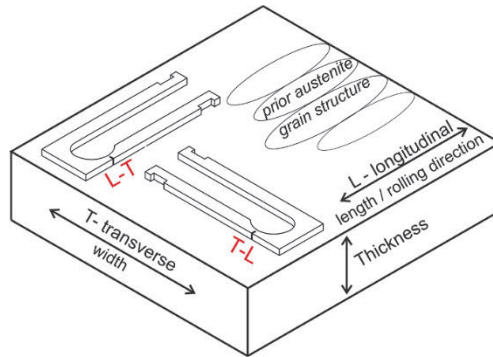


Fig. 9. Tuning-fork specimen orientations utilized in Publications III – IV. (Adapted, with permission, from Publication III © 2020 AMPP GLOBAL CENTER, INC).

According to the results of the tensile tests, FEM models were designed with Abaqus for each steel grade. The models were used to investigate the outer part of the narrower side of the specimen arm where tensile stress concentration is created by compressing the specimen arms towards each other. During tests, stress concentration is controlled by the arm displacement with a specially designed clamp, making the tuning-fork test a constant displacement test. Arm displacement also creates compressive stress on the inner part of the narrower arm, but it is not relevant in terms of crack initiation. Fig. 10 presents clamped specimens with highlighted stress concentration regions. With unnotched and notched specimens, stress concentration is always in the elastic region. Unnotched specimens were clamped with various stress levels (Publications I – III), and notched tuning-forks had only one maximum stress level of 1000 MPa (Publication IV).

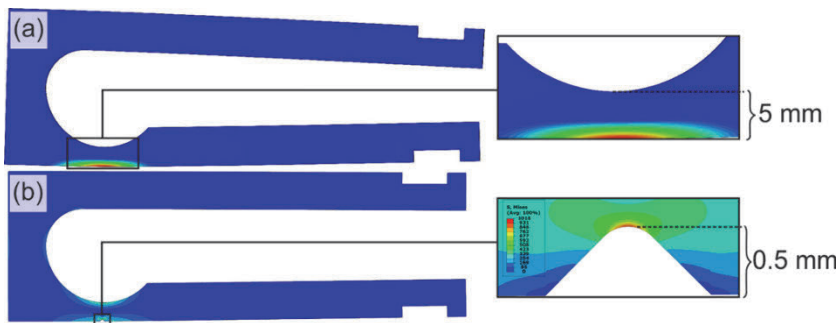


Fig. 10. Normalized stress state of (a) an unnotched and von Mises stress distribution, and (b) of notched tuning-fork specimens with red colour indicating highly stressed regions.

In Publications I – II, clamping was conducted with a simple clamp, which adjusted the arm distance with a clamping screw. The interpretation of the results was based on testing different stress levels and finding a relative threshold stress level below which cracking did not occur. The known shortcoming of this type of constant-displacement or constant load test is the relatively long testing time, since all specimens are not assured to fail [3], [31]. In Publications I – II, this was the case with the determination of threshold stress, and therefore the pragmatic approach was to select the 24 h time limit for one test. Also, the test results did not provide any additional information regarding the cracking mechanics apart from fracture surfaces.

Therefore, the clamping was further developed in Publications III – IV, where loadcell was integrated inside the clamp to be able to monitor different crack propagation stages and eliminate the time uncertainty of the tests. Loadcell produced time-Force (t-F) data, which was processed with a specially designed graphical user interface (GUI) tool called Freader, shortened from Force-reader, in the following order:

1. Removal of unnecessary data fluctuation by applying a specific moving point average.
2. Calculation of crack initiation time (t_i) and time-to-fracture (t_f) with limiting angle principle (5°).
3. Calculation of crack propagation time ($t_f - t_i$) and average crack propagation rate (CPR).

The 5° limiting angle means the angle between the start/end line value and the force data. The line was drawn based on the first/last data points (Publication III) or based on the average of multiple data points from the start/end (Publication IV). The GUI tool automatically compares the changing angle between the line and the following/previous data. The force data point at which angle is 5° versus the compared initial value was marked t_i or t_f . Average CPR is determined based on the difference between t_f and t_i , which was divided by the crack length.

With notched specimens (Publication IV), a single crack was formed during each test and CPR was possible to calculate. In the designed geometry, the original ligament is 4.5 mm, but the cracks never propagated through the specimen, so the actual crack length was 4.2 – 4.4 mm. Therefore, a small remaining ligament was broken by hand after each test and measured for accurate calculation of the average CPR. Macro- and microscopic investigations were conducted for the obtained

fracture surfaces, which were cut from the TFT specimens after a fracture. Fig. 11 presents an example of the t-F data and fracture surfaces.

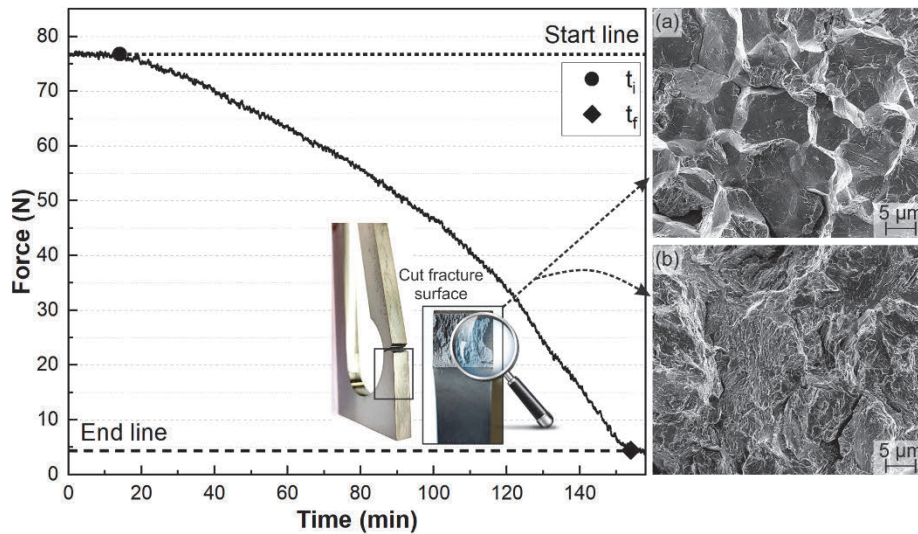


Fig. 11. Example of t-F data and (a) intergranular and (b) transgranular fracture surfaces.

In addition to the clamping arrangement, three different cells were utilized in hydrogen charging, which gradually evolved from a small beaker to a bigger cell assembly. The original cell contained only a taped specimen as WE, a CE, and electrolyte. The electrolyte was poured until taping marks and there was no additional electrolyte circulation. Without RE, only constant current density could be applied, and therefore the original set-up was galvanostatic (Publication I). For the next Publications, the set-up was developed to be used for potentiostatic hydrogen charging. RE was added to the set-up, along with a removable cap for all electrodes and electrolyte circulation. In cell version 2, the electrolyte was circulated so that the flow velocity was controlled by additional stopcocks. The electrolyte was pumped at a constant rate from above, and it dripped out of the cell at the same speed from a stopcock-controlled bottom outlet. This allowed for maintaining approximately the same electrolyte level during hydrogen charging. In cell version 3, the circulation was changed so that the electrolyte was pumped to the bottom of the cell and excess electrolyte automatically flowed over through an upper outlet maintaining the same electrolyte level. The evolution of the cells is

presented in Fig. 12, and specific information regarding specimens, clamping, and charging conditions for each Publication is summarized in Table 2.

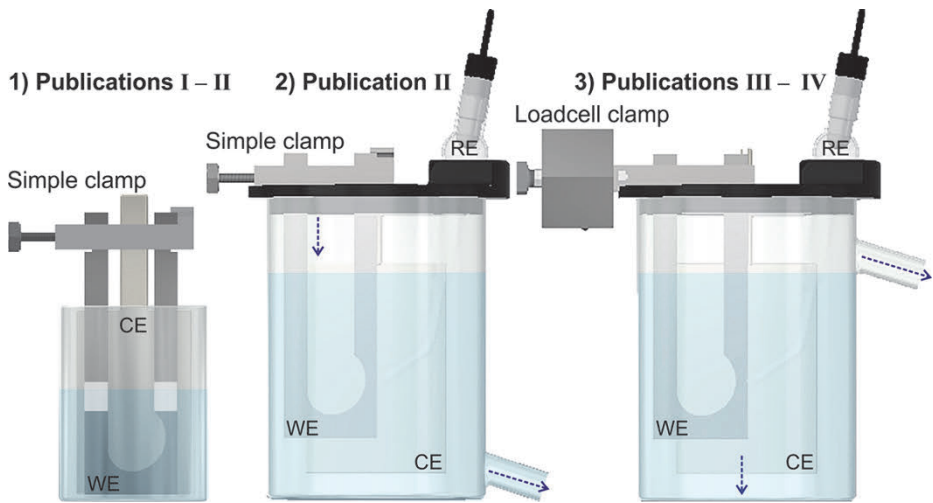


Fig. 12. 3D models of all utilized cells, with markings for electrodes and electrolyte circulation.

Table 2. Specimens, clamping, and hydrogen charging arrangements of each Publication.

Publication	I	II	III	IV
Specimen type	Unnotched	Unnotched	Unnotched	Notched
Specimen orientation	L-T	L-T	L-T and T-L	L, T and not considered
Clamp	Simple	Simple	Loadcell	Loadcell
Applied stress (elastic)	Threshold stress level	Threshold stress level	1/3 – 2/3 R_m	1000 MPa
Electrolyte	0.1M H_2SO_4 + 5 g/l CH_4N_2S	0.1M H_2SO_4 + 5 g/l CH_4N_2S	0.1M H_2SO_4 + 5 g/l CH_4N_2S	0.1M H_2SO_4 + 1 g/l CH_4N_2S
Hydrogen charging conditions	Galvanostatic	Galvanostatic and potentiostatic	Potentiostatic	Potentiostatic
Current density (-)	10 mA/ cm^2	10 mA/ cm^2		
Potential (-)		1200 mV	1200 mV	1200 mV
CE	MMO mesh	Coated Ti mesh	Pt coated Ti plate	Pt coated Ti plate
RE	-	Hg/Hg ₂ SO ₄	Hg/Hg ₂ SO ₄	Hg/Hg ₂ SO ₄

3.2.2 Hydrogen permeation tests

To complement the tuning-fork tests, electrochemical hydrogen permeation tests (EP) were conducted in the last Publication IV utilizing the standard Devanathan-Stachurski (DS) method. According to ASTM G148 – 97 and SFS-EN ISO 17081, the permeation apparatus needs to consist of two separate cells that are inert to the test environment. However, there are no specific instructions on how to build it or clamp the cells together without leakage [61], [62].

The preliminary testing was conducted with a commercial version of the permeation cell, but it was found to be impractical and deficient in sealing with a traditionally used pinch clamp due to easily occurring misalignment of the sealing rings/cells/specimen. The cell geometry also led to the formation of air gaps on the specimen surface during hydrogen charging and therefore caused corrosion of the specimens. To address all the above-mentioned challenges, a new permeation apparatus was specifically designed and built by the author. The final apparatus consisted of geometrically enhanced glass cells, an easy and leak-proof sealing/clamping system, and electrode covers (Fig. 13). The spherical joints of the glass cells were designed so that the inner diameter increases towards the main cell. Together with mixing, this design facilitates bubble removal and eliminates air gaps that can cause unwanted corrosion on the specimen surface. For sealing, removable plastic collars with O-rings on both sides are locked on glass flanges. The cells are then positioned on a holder where only horizontal movement is allowed to avoid misalignment during clamping. The plastic clamp is then put on top of spherical joints and the specimen is clamped between the collars with a 4-screw system that applies evenly distributed pressure.

The ready EP test set-up consisted of two potentiostats and a two-compartment glass cell with a steel specimen clamped between them acting as WE. Each cell has a plastic cover with holes for CE (Pt coated Ti mesh), SCE as RE, and an inlet for N₂ bubbling. During EP tests, 0.1 M NaOH solution was used on both sides of the permeation cell. On the left side with hydrogen charging, the deaerated electrolyte was constantly pumped at the bottom of the cell and the excess electrolyte flowed over from an outlet located at the top of the cell, which maintained the same electrolyte level.

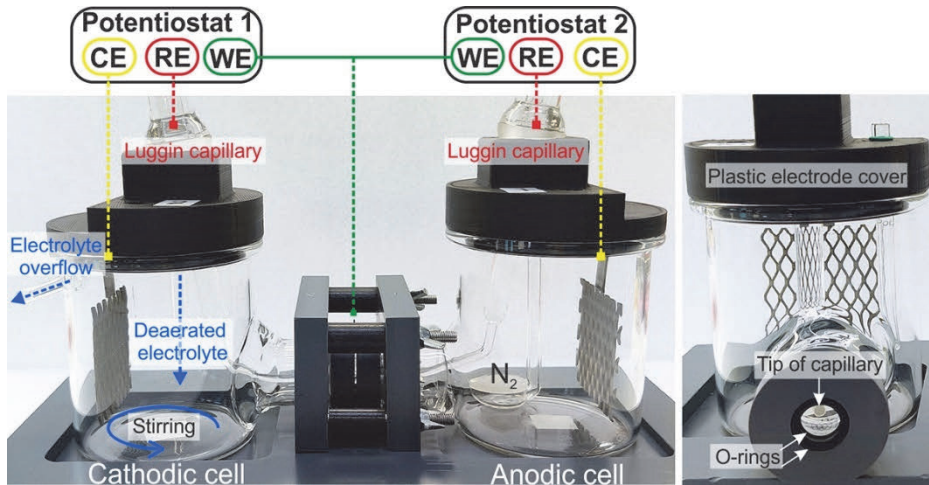


Fig. 13. Permeation cell utilized in EP experiments. (Reprinted, with permission, from Publication IV © 2022 Authors).

The first step of the test is specimen preparation. Steel specimens (40x35x1 mm) were first mirror-polished (3 μm diamond) from both sides, followed by the taping of one side. The untaped surface was repolished and immediately electroplated with palladium (Pd) to achieve approximately 1 μm coating thickness. The electroplating was conducted with a commercial palladium bath containing 6 g/l Pd [63]. After coating, taping was removed, and the steel side repolished, followed by immediate clamping of the specimen between the two cells. The Pd-coated surface faced the right side of the cell, which was filled with electrolyte, and a constant anodic potential of 0.3 V was applied while the left side was kept in inert conditions with N_2 . As soon as the background current decreased to 0.1 – 0.3 $\mu\text{A}/\text{cm}^2$ (1 – 2 h), the left side of the cell was also filled with electrolyte and constant potentiostatic hydrogen pre-charging with -1.2 V was started. During charging, the permeation current density was recorded on the right side of the cell as a function of time until it reached a steady-state value (12 h). Decay and build-up transients were then determined by lowering (-1.1 V) and increasing the hydrogen charging potential (-1.2 V) two times. After the last/second build-up transient, the left side was polarized with 0.3 V until complete decay. On both sides, 4 readings/s were utilized during the permeation test.

For fast result analysis and easy fitting, the GUI tool Permeator was developed. Each permeation curve was uploaded to Permeator with the mention of specimen thickness. As in Freader, a moving point average could be applied if necessary. The

permeation curve was then divided into sections that had separate fitting curves, which could be modified by adjusting time and permeation current density.

The sections from decay and build-up curves are used to calculate diffusion coefficient (D) with a refined successive transient method [34] as well as subsurface hydrogen concentration (C_H). The last, complete decay curve is used to evaluate the reversible trapping site density (N_T) of investigated steel grades [33], [36], [64]–[69]. D is calculated with Equation 1 (build-up) and Equation 2 (decay)

$$\frac{i_p - i_p^0}{i_p^\infty - i_p^0} = \frac{2L}{\sqrt{\pi Dt}} \sum_{n=0}^{\infty} \exp\left(-\frac{(2n+1)^2 L^2}{4Dt}\right) \quad (1)$$

$$\frac{i_p - i_p^\infty}{i_p^0 - i_p^\infty} = 1 - \frac{2L}{\sqrt{\pi Dt}} \sum_{n=0}^{\infty} \exp\left(-\frac{(2n+1)^2 L^2}{4Dt}\right), \quad (2)$$

where L = specimen thickness, i_p = measured permeation rate at time t , i_p^0 = initial hydrogen permeation rate ($t = 0$), and i_p^∞ = new steady-state permeation rate ($t \rightarrow \infty$). C_H of Equation 3 is

$$C_H = \frac{i_\infty L}{FD}, \quad (3)$$

where i_∞ = steady-state permeation current and F = Faraday constant. N_T (sites/cm³) of Equation 4 is

$$N_T = \frac{2A \cdot 6.24 \cdot 10^{18}}{L}, \quad (4)$$

where A = area difference between the complete decay and theoretical permeation transients (As/cm²), L = specimen thickness (cm), and $6.24 \cdot 10^{18}$ is the number of hydrogen traps ($1 \text{ C} = 1 \text{ As} = 6.24 \cdot 10^{18} \text{ e}$).

3.3 Materials characterization

For microstructural categorization, steel specimens were cut, hot-mounted, polished, and etched with 2% nital or with a picric acid solution (1.4 g picric acid + 100 ml distilled water + 1 ml wetting agent + HCl drops). The nital etchant revealed the martensitic microstructure, and the picric acid solution the PAG boundaries. The martensitic microstructures were examined with a Zeiss Sigma field emission scanning electron microscope (FESEM), and the PAG structures were studied with an optical or laser microscope.

Fracture surface analyses were conducted for tuning-fork specimens after the tests. First, specimens were taken out of the corrosion cell, rinsed with water, and ultrasonically cleaned with ethanol. The area of interest was cut, and the fracture surface was treated with a specific solution (50 ml HCl, 450 ml distilled water, and 15 g hexamethylene-tetramine) to remove possible corrosion products. Fracture surfaces were first macroscopically examined, followed by microscopic studies with FESEM. Some of the fracture surfaces were also treated with plasma (Plasmalab 80 Plus) for 10 min to achieve a better surface quality.

With interrupted tuning-fork tests, the notched area was cut, ultrasonically cleaned in ethanol, and subsequently mounted and polished. Polished specimens were plasma-cleaned for electron backscatter diffraction (EBSD) analysis. The small, initiated cracks contained tiny organic particles after polishing, which could not be removed by simple ultrasonic cleaning. If specimens were put in vacuum conditions, e.g., FESEM, the organic matter would contaminate the investigated region. Therefore, plasma cleaning was extremely important since it combined simultaneous vacuum conditions and removal of the organic particles. After EBSD, specimens were repolished and etched to reveal the PAG structures, followed by microscopical examinations with optical or laser microscopes.

4 Results and discussion

This part of the thesis contains the main results and discussion from Publications I – IV divided by different stages of tuning-fork test development. Throughout all Publications, one of the main results and novelty lies in the developed testing method, which allows ranking of the test materials.

The novel tuning-fork test was first used in Publications I – II for simplified steel ranking to assure that the results are valid in terms of the known principles such as “higher strength leads to a higher hydrogen susceptibility”. In Publications III – IV, loadcell was added to the clamping system which provides consistent data regarding crack initiation, crack propagation, and time-to-fracture. In Publication IV, the modified notch specimen geometry allowed a more profound study of the cracking mechanism, as sufficient stress-concentration facilitated single crack initiation and propagation during the test. With loadcell clamping, the tuning-fork test was utilized in studying the PAG structure of ultrahigh-strength steels and complimented with traditional electrochemical hydrogen permeation tests, which is the last part of this chapter.

4.1 Relative threshold stress level

In Publications I – II, the comparison of the steel grades is based on the binary search procedure, and the determination of the lowest fracture and no-fracture stress results with a 25 MPa difference [70]. The mechanical properties of the investigated steel grades according to their Publication are given in Table 3.

Table 3. Mechanical properties of the test materials in Publications I – II.

Steel (HBW)	Measured hardness (HBW)	0.2% offset yield stress = YS (MPa)	Tensile strength = TS (MPa)	Publication
300	270	780	940	II
400	400	1110	1250	II
450	440	1190	1470	I
500 ₁	500	1440	1630	I
500 ₂	490	1410	1630	II
550	580	1770	2060	II
600	600	1760	2090	I

In Publication I, the novel tuning-fork testing method is used to calculate a relative threshold stress level (σ_{th}/R_m) of 450, 500, and 600 HBW steels with L-T oriented specimens. Threshold stress (σ_{th}) is determined by calculating the average of the lowest fracture and no-fracture values (σ_{th}). Relative threshold stress is material-specific, and is determined by dividing the obtained σ_{th} by the tensile strength of the material (R_m). Relative threshold stress level results are presented in Fig. 14. It is general knowledge that steels have greater susceptibility to hydrogen with increasing strength levels. Therefore, the obtained results are reasonable as σ_{th}/R_m lowers with increasing hardness.

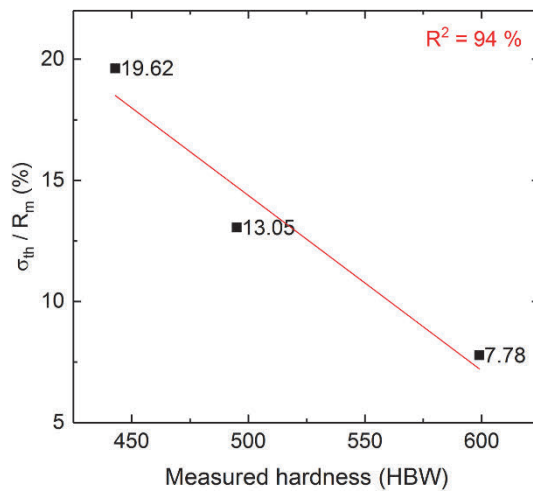


Fig. 14. Correlation between relative threshold stress level and steel hardness. (Reprinted, with permission, from Publication I © 2018 WILEY-VCH Verlag GmbH & Co. KGaA, Weinheim).

The testing environment of sulfuric acid is considered to mimic hydrogen-induced stress corrosion cracking as it is simultaneously corrosive and there occurs hydrogen evolution. After hydrogen charging, pitting corrosion was observed on the specimen surfaces. Most likely, the observed pitting corrosion resulted from near-surface inclusions, e.g., sulphide inclusions, which acted as potential crack initiation sites [71]–[73]. Crack initiation sites were detected at the pits, and there was also crack branching, which is usually considered a sign of hydrogen-induced stress corrosion cracking. Fig. 15 presents crack initiation at a pit and branching features of crack propagation.

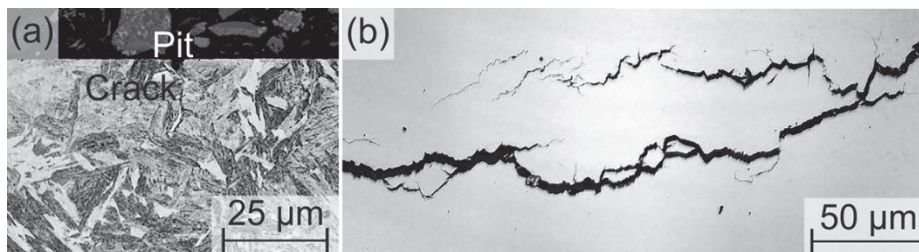


Fig. 15. (a) crack initiation at a pit, and (b) branched crack propagation morphology of 600 HBW steel (Adapted, with permission, from Publication I © 2018 WILEY-VCH Verlag GmbH & Co. KGaA, Weinheim).

Steel categorization is continued in Publication II by using the same electrolyte for galvanostatic and potentiostatic hydrogen charging of 300, 400, 500₂, and 550 HBW materials with L-T specimens. All steel grades except 500 HBW were selected to complement Publication I by testing additional hardness levels, such as the softer 300 HBW and 400 HBW materials.

The softer steel grades do not manifest a high susceptibility to hydrogen. With the 300 HBW steel, cracking did not occur at all with potentiostatic charging, and with 400 HBW steel, both charging results are inconclusive due to overlapping fracture and no-fracture values. Test conditions were considered severe with the galvanostatic set-up because hydrogen blisters were observed on the surface of the 300 HBW steel. Also, similarly to Publication I, pitting corrosion was visible on the specimen surface after hydrogen charging. Fig. 16. presents an example of the pitting corrosion of 500 HBW steel and hydrogen blistering of 300 HBW steel.

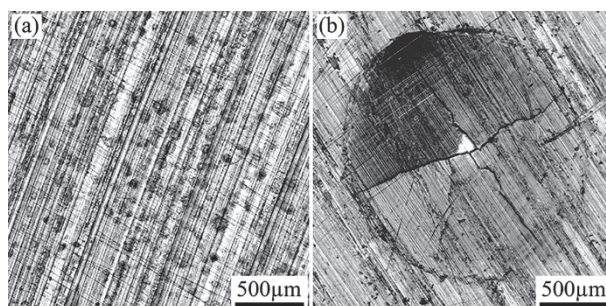


Fig. 16. Example of (a) pitting corrosion (500 HBW), and (b) a hydrogen blister (300 HBW) observed after hydrogen charging (Reprinted under CC BY 4.0 license from Publication II © 2020 Authors).

On the other hand, the test results of steels with higher hardness and strength (500 – 550 HBW) show good reproducibility, which indicates that steels with less than 400 HBW hardness are not susceptible enough to HE in the given test conditions. Generally, both charging conditions produce similar results, which are summed up in Fig. 17 as applied stress/ R_m . The graphs present all fracture and no-fracture data without repetitions for the clarity of the graph.

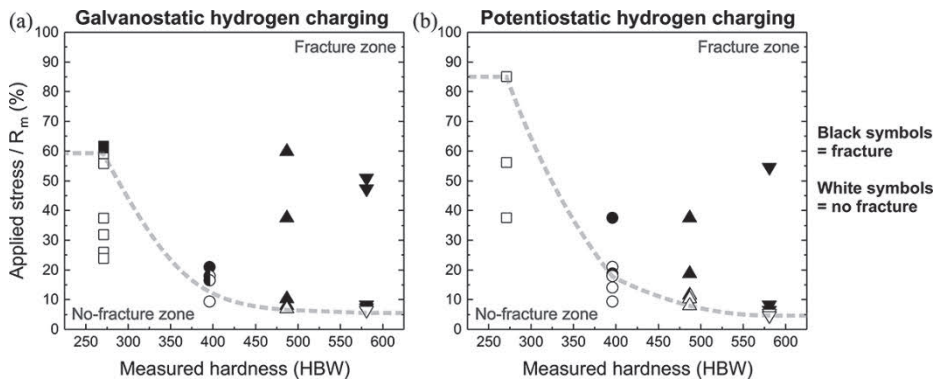


Fig. 17. Comparison of fracture and no-fracture results of (a) galvanostatic, and (b) potentiostatic test set-up (Reprinted under CC BY 4.0 license from Publication II © 2020 Authors).

A closer examination shows that potentiostatic hydrogen charging produces larger differences in the lowest fracture stress, and therefore, has a better resolution. One reason for differences in resolution can be the superior potential control in potentiostatic hydrogen charging, which assures the same hydrogen activity in the specimens. Also, the charging potential of -1200 mV provided less hydrogen in comparison to the constant current density of -10 mA/cm², which minimizes damages to the charged surface and therefore provides more beneficial testing environment. Based on these results, potentiostatic hydrogen charging was selected for the following tuning-fork testing.

The tuning-fork test method is capable of detecting HE susceptibility differences based on the results presented in Publications I and II. Susceptibility to HE increases with the increasing hardness, which is expected for ultrahigh-strength steels. There are significant differences in HE susceptibility when large changes in the hardness are involved, but there was no way to compare steels with the same hardness level using TFT. Intending to investigate microstructural effects, specifically PAG structure, further test development was required.

The observed phenomena in Publications I – II were caused by hydrogen-induced stress corrosion cracking, but in the following Publications III – IV, the cracking is referred to as hydrogen-induced fracture, which implies hydrogen embrittlement as the main degradation mechanism.

4.2 Crack propagation phases

4.2.1 Unnotched specimens

In Publication III, the most important addition was the integration of a loadcell inside the clamp. The integrated loadcell clamping completely changed the interpretation of the results, because it allowed monitoring of all crack propagation stages during the test. This also led to the development of a separate GUI tool (Force-reader = Freader) for fast analysis of the test results, allowing the systematic calculation of crack initiation time (t_i), propagation time (t_p), and time-to-fracture (t_f) for multiple tests at the same time. Different types of graphs were produced depending on the stress level. The profound explanations for the analysis of each graph type as well as the selection and calculation of suitable parameters for result analysis are explained in Publication III.

Because of the addition of the loadcell, it is now possible to detect differences between the materials with similar mechanical properties and microstructure, meaning that also the PAG structure investigation is possible. The first test materials selected for the comparison were three 500 HBW steels, which have similar mechanical properties but different alloying and production routes (DQ and RQ). Two steels are direct-quenched (DQ₁ and DQ₂) with different degrees of PAG pancaking, and one is reheated and quenched (RQ) with an equiaxed PAG structure. The direction of elongated PAG structure in terms of crack propagation had to be considered because of the microstructural anisotropy of DQ steels. Therefore, both L-T and T-L specimen types were investigated.

Table 4 presents the mechanical properties and grain size information of the test materials, such as mean PAG size (d_G), grain boundary surface area per unit volume (S_V), and RD/ND grain size ratio. Fig. 18 presents the PAG structure of each material in the RD-ND direction.

Table 4. Mechanical properties and grain size information of the test materials (Adapted, with permission, from Publication III © 2020 AMPP GLOBAL CENTER, INC).

Steel grade	Measured hardness (HBW)	0.2% offset yield stress = YS (MPa)	Tensile strength = TS (MPa)	YS/TS	d_G (μm)	S_v (mm^2/mm^3)	RD/ND
DQ1	490				10	272	3.0 \approx 3
L-T		1410	1630	0.86			
T-L		1380	1630	0.85			
DQ2	500				15	151	1.6 \approx 2
L-T		1400	1580	0.89			
T-L		1420	1640	0.86			
RQ	510				10	208	1.1 \approx 1
L-T		1470	1650	0.89			
T-L		1430	1650	0.86			

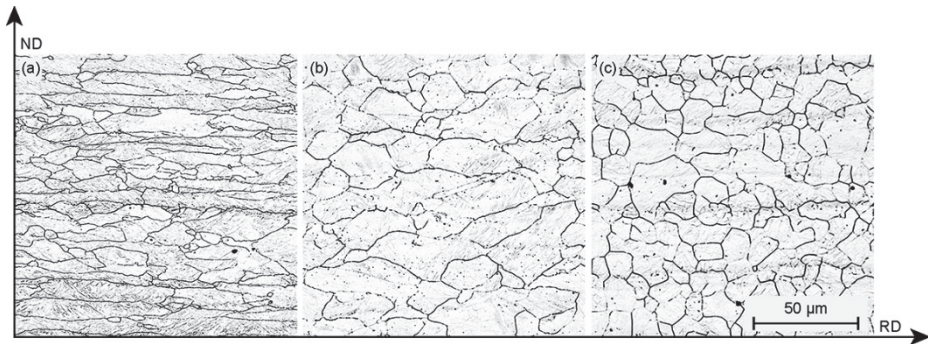


Fig. 18. PAG structure of investigated steel grades. (a) DQ, (b) DQ, and (c) RQ (Reprinted, with permission, from Publication III © 2020 AMPP GLOBAL CENTER, INC).

Same potentiostatic charging conditions were applied as in Publication II but with three different elastic stress levels: $1/3 R_m$, $1/2 R_m$, and $2/3 R_m$, where R_m stands for tensile strength of the material ($R_m = TS$). The results from stress levels $1/2 R_m$ and $2/3 R_m$ are compared when $1/3 R_m$ could not be used for steel ranking because of poor reproducibility of the tests and high scatter in results. Therefore, at this development stage of the tuning-fork test, the known shortcoming of the test is the inability to utilize a wider range of elastic stresses.

17% of the tests with DQ_2 resulted in premature failure, and fracture surfaces of the shorter tests have a rough, irregular appearance. DQ_2 has higher Mn and S contents in comparison to other materials, and therefore abrupt fractures most likely

resulted from MnS centreline segregation. The anomalous tests are not taken into consideration in further result analysis. Depending on the applied stress level, several cracks are visible on the specimen surface at the highest stress level, producing the highest number of cracks (Fig. 19). The lowest stress level $1/3 R_m$ produced usually only one crack, but unfortunately, it cannot be used for material comparison due to the high scatter in the results.

It is not possible to calculate the average CPR with unnotched specimens since it would not describe the crack growth rate of a single crack. This led to the idea of a new notched tuning-fork specimen geometry with a more concentrated stress region, aiming to produce only one crack during tests for CPR calculation.

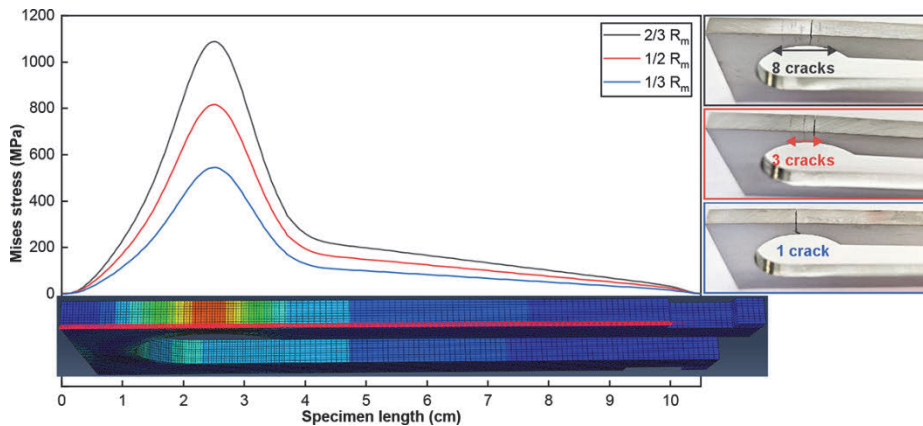


Fig. 19. The dependency of applied stress level on the number of cracks (Reprinted, with permission, from Publication III © 2020 AMPP GLOBAL CENTER, INC).

Microstructural anisotropy is investigated by comparing L-T and T-L specimens of the same steel. DQ steels have an evident difference in t_f depending on specimen orientation, but RQ steel does not manifest a statistically significant deviation in the results. Because of the elongated PAG structure, there are a lot more grain boundaries to traverse if crack propagation proceeds transverse to the rolling direction. This explains the longer t_f results of the L-T specimens. No orientation differences are observed with the more symmetrical PAG structure of RQ steel. The differences between L-T and T-L specimens of DQ steel indicate that it is important to consider the possible crack plane of hydrogen-induced cracks during the structural design of applications meant for hydrogen-containing environments.

A final comparison of the steel grades with both stress levels shows that DQ₁ with the highest degree of pancaking performs best, followed by DQ₂ with a less elongated structure, and RQ having the shortest t_f (Fig. 20). Each presented column has marked proportions of initiation time, propagation time, and final force drop. The final force drop results from the coalescence of opposite cracks at the end of the test, and it was observed as a sudden drop in the force values. No significant differences are observed between the stress levels, which is most likely caused by simultaneous propagation of multiple cracks.

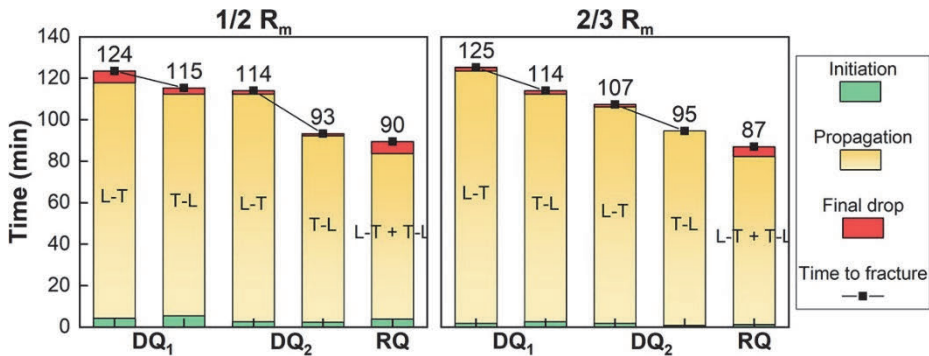


Fig. 20. Time-to-fracture results at 1/2 and 2/3 R_m stress levels and average proportions of crack initiation, propagation, and final force drop regions of each steel (Reprinted, with permission, from Publication III © 2020 AMPP GLOBAL CENTER, INC).

Fracture surface examination reveals differences between the failure behaviour of DQ and RQ steels. DQ steels have predominately transgranular quasi-cleavage fracture surfaces, while RQ steel shows pronounced intergranular crack propagation. However, there are no planar grain boundary surfaces, which suggests that the crack propagation may have occurred in the close vicinity of the grain boundaries in RQ steel. Yamasaki et al. stated that in steels rolled in the non-recrystallization region, large stress does not act at the grain boundaries when stress is applied parallel with elongated austenite grains, and therefore quasi-cleavage cracking occurs [74]. This is accurate for DQ steels tested in the L-T direction. Fig. 21 presents a general and detailed view of the fracture surfaces. The results indicate that elongated PAG structure is beneficial in lowering the susceptibility to hydrogen embrittlement because of longer t_f times and the transgranular crack propagation. The shorter t_f of RQ steel also suggests that the intergranular crack propagation is more detrimental than transgranular.

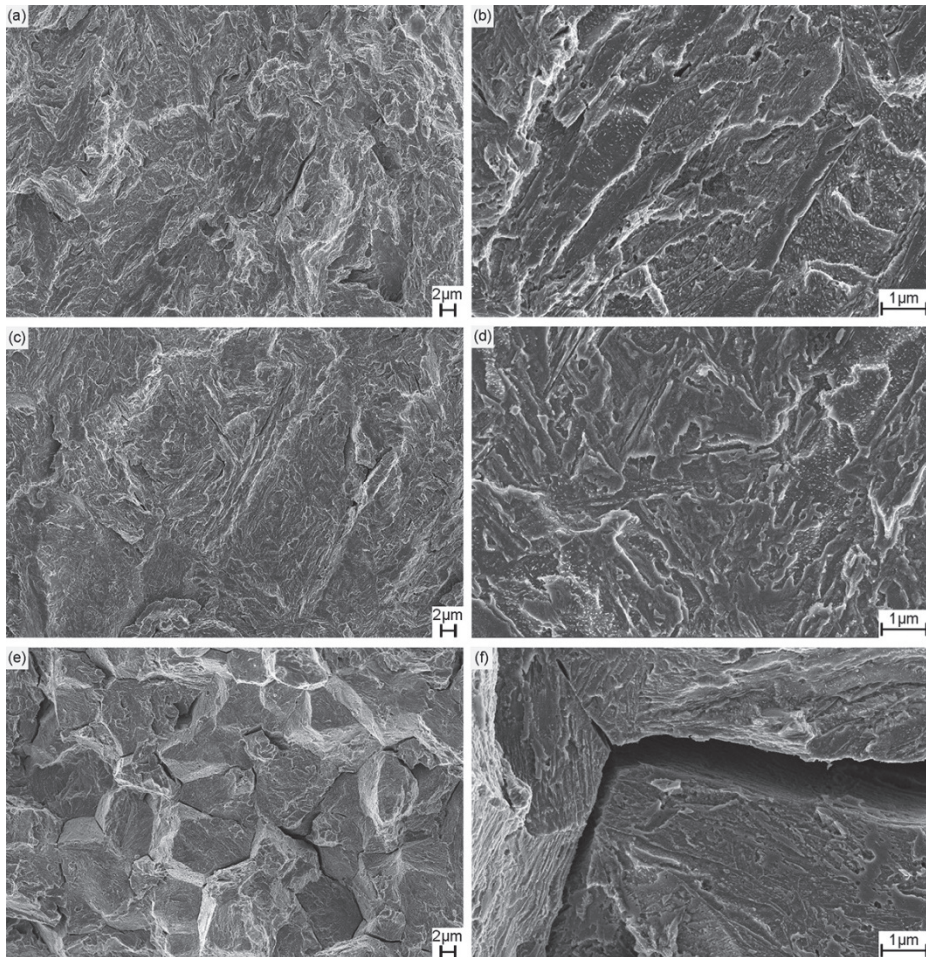


Fig. 21. Fracture surfaces of (a, b) DQ₁, (c, d) DQ₂, and (e, f) RQ. Notice the scale. (Reprinted, with permission, from Publication III © 2020 AMPP GLOBAL CENTER, INC).

The obtained results cannot be solely contributed to the differences in PAG structures because many other factors also affect this comparison. The production routes of DQ and RQ steels are different, which can lead to different grain microstructures (laths, blocks, packets), amount of retained austenite, and dislocation densities. Combined with different alloying, there are also changes in the degree of auto-tempering, i.e., carbide structure, which includes, e.g., cementite, η and ϵ carbides. All the above-mentioned factors are highly important in the

evaluation of HE susceptibility because they affect hydrogen diffusion as well as hydrogen trapping properties. Different alloying also leads to a different amount of embrittling elements and grain boundary segregation, which can be directly linked to intergranular crack propagation.

Therefore, to isolate the effects of PAG structure as the main investigated parameter, a more precise comparison is required. For this, steels with the same alloying but different PAG structures should be compared. This is achieved in the final publication, Publication IV, where the same direct-quenched steel as in Publication III (DQ₁) is re-austenitized at two different temperatures and subsequently quenched to produce equiaxed PAG structures with two different grain sizes. The new comparison allows the investigation to focus on the effect of PAG structure with the other differences in the microstructure and mechanical properties minimized.

4.2.2 Notched specimens

Three 500 HBW steels with identical alloying but different PAG shapes and sizes are studied with tuning-fork tests. DQ is the same material as DQ₁ from Publication III, A860 represents DQ steel which was re-austenitized at 860 °C and quenched, and the same for A960 but with 960 °C austenitization temperature. DQ has an elongated PAG structure, while A860 and A960 have an equiaxed PAG structure with different grain sizes. Higher austenitization temperature produced four times bigger PAG size in A960 in comparison to A860 and DQ, which allows the comparison of both shape and size of the PAG structure. The steels have fully martensitic structures, with a negligible amount of retained austenite (< 1%) estimated by XRD analysis. With the same alloying, the steels also have the same amount of grain boundary impurity elements, but their local concentrations can differ after re-austenitization. Fig. 22 presents the PAG and carbide structure of the test materials.

Microstructures were also studied with EBSD, which shows a slightly higher fraction of low-angle boundaries for DQ steel in comparison to A860 and A960 steels. The substructure of DQ steel has more crystallographic discontinuities or nucleation sites for martensite in comparison to strain-free austenite (A860 and A960) [24], [25]. Therefore, the higher fraction of low-angle or lath boundaries of DQ steel results from the different manufacturing methods. However, the block size of all steel grades is approximately the same (1.7 μm). The IPF images with the distribution of grain boundary misorientation angles are presented in Fig. 23.

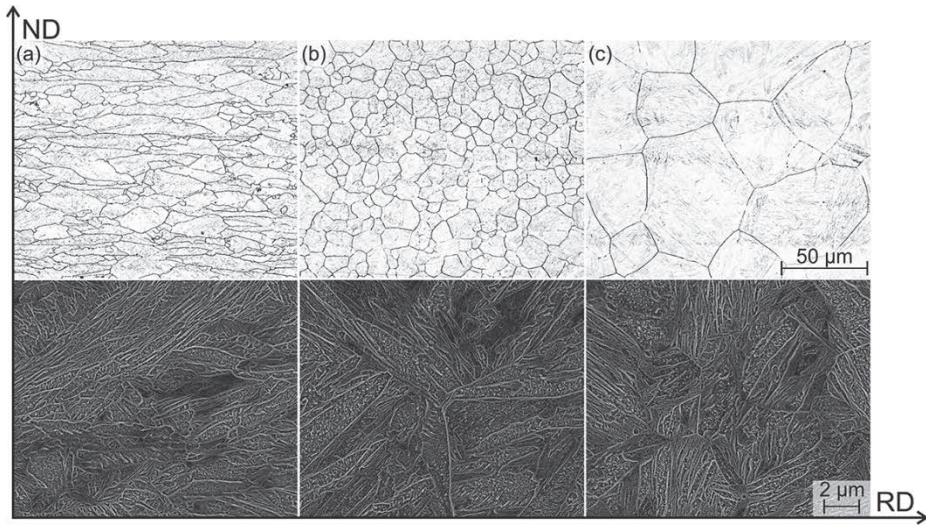


Fig. 22. PAG and carbide structure of investigated steel grades. (a) DQ, (b) A860, and (c) A960. (Adapted, with permission, from Publication IV © 2022 Authors).

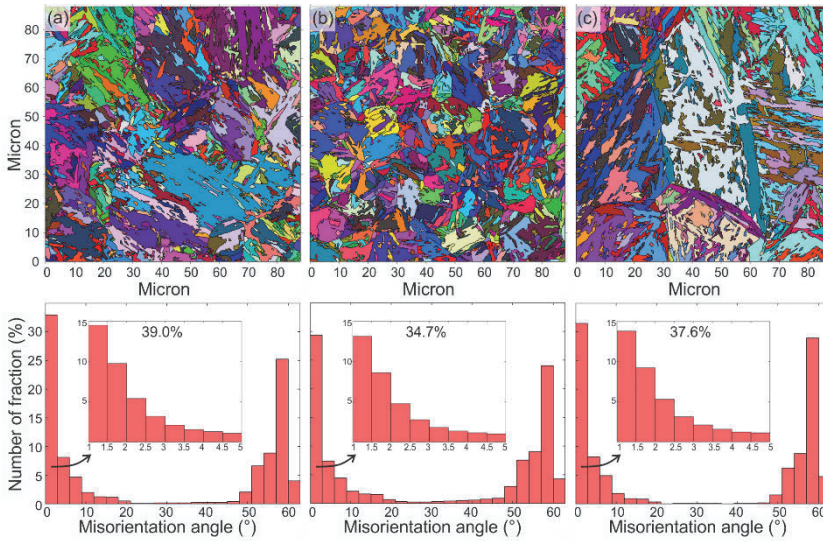


Fig. 23. IPF images and grain boundary misorientation angle distribution of (a) DQ, (b) A860, and (c) A960. (Reprinted, with permission, from Publication IV © 2022 Authors).

The average PAG size of DQ steel depends on the specimen orientation, and therefore both L and T directions are considered. With re-austenitized steels, specimen orientation is random because our previous results from Publication III showed no significant differences between L-T and T-L specimens with equiaxed PAG structure. Table 5 summarizes the mechanical properties and PAG characteristics of each steel. The test materials have similar tensile strength and hardness, but DQ steel has a higher YS in comparison to the re-austenitized steels, which indicates that DQ steel has a higher dislocation density.

Table 5. Mechanical properties and PAG characteristics of investigated materials. (Adapted, with permission, from Publication IV © 2022 Authors).

Steel grade	Measured hardness (HBW)	YS (MPa)	TS (MPa)	YS/TS	A _{gt} (%)	d _G (μm)	d _G (crack plane)	S _v (mm ² /mm ³)	RD/ND
DQ	484 (±2.7)					10		270	3
L		1410	1630	0.86	6.9		7.5		
T		1380	1630	0.85	3.3		9		
A860	482 (±2.1)					9		221	1
L		1150	1580	0.73	5.2		9.5		
T		1160	1600	0.73	4.9		9.3		
A960	475(±2.2)					43		46	1
L		1100	1530	0.73	4.9		42.6		
T		1100	1530	0.72	4.7		43		

Notched tuning-fork specimens are tested in a similar hydrogen charging environment (0.1 M H₂SO₄ + 1 g/l thiourea) as in previous Publications, but with a decreased amount of thiourea. Also, instead of the utilization of different stress levels in the elastic region, one stress level was selected that could be used to compare all three materials.

The selected stress level of 1000 MPa and corresponding 1.49 mm arm displacement are utilized in all tests to provide the same driving force for crack initiation. Utilized displacement was assured not to cause plastic deformation for any of the test materials. Fig. 24 presents the Mises stress distribution along the bottom of the notch and time-stress distribution during clamping with 1000 MPa. Since the corners of the notch have slightly higher stress, they are likely acting as primary crack initiation sites.

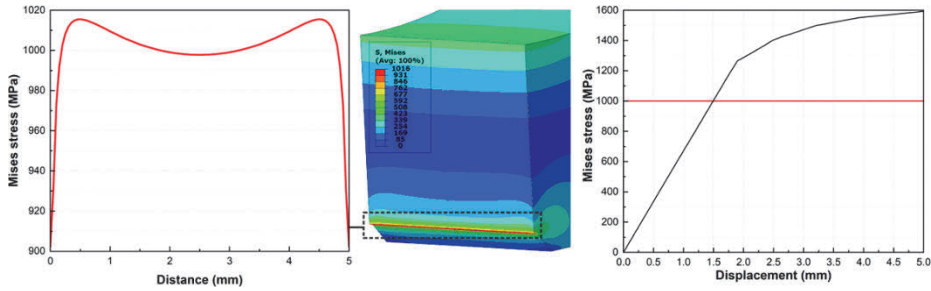


Fig. 24. Mises stress distribution along the notch thickness and required displacement when stressed at 1000 MPa. (Reprinted, with permission, from Publication IV © 2022 Authors).

With 1000 MPa stress, the initial force for all tests is in the range of 68 – 81 N. Fig. 25 presents all obtained t-F data. For DQ steel, t-F curve shapes are very similar with a plateau region (initiation) followed by gradually decreasing force values (propagation). For re-austenitized steels, the curve shapes differ with the abrupt ending of crack propagation, which shortens time-to-fracture results. From each curve, t_i and t_f values are determined and average CPR as well as maximum CPR are calculated for evaluation of susceptibility to HE.

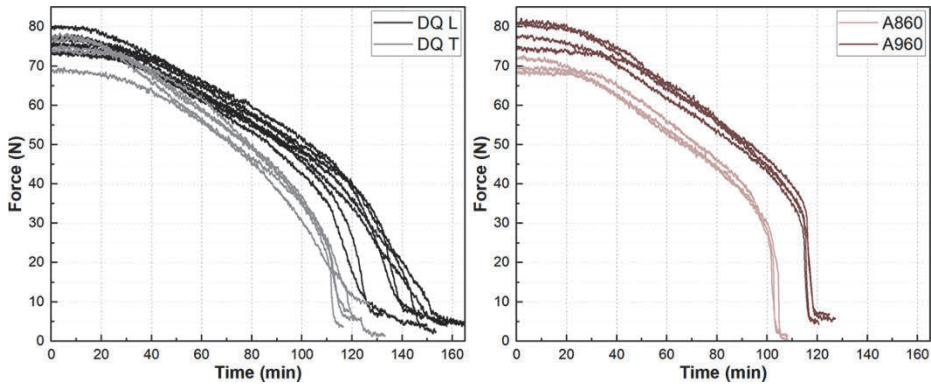


Fig. 25. t-F data of recorded tuning-fork tests. (Reprinted, with permission, from Publication IV © 2022 Authors).

Fig. 26 presents t_i and t_f values, and Fig. 27 presents the obtained CPR results. There are no statistically significant differences for t_i ($p = 0.05$), which is explained by the similar driving force, i.e., arm distance, applied in all tests. However, significant differences are detected for t_f , and therefore CPR can be used for steel

comparison. From tested materials, DQ L has the best performance because of the slowest average CPR. In Publication III, the same test material DQ steel showed enhanced performance in comparison to other steels with less elongated or equiaxed PAG structure. DQ T and re-austenitized steels have faster CPR and differences are significant ($p = 0.05$) in comparison to DQ L. There are also big differences for maximum CPR, where re-austenitized steels have 3 – 4 times faster values in comparison to DQ steel (both directions). Maximum CPR reflects on the abrupt ending in t-F curves and suggests that the equiaxed PAG structure has a different type of crack propagation.

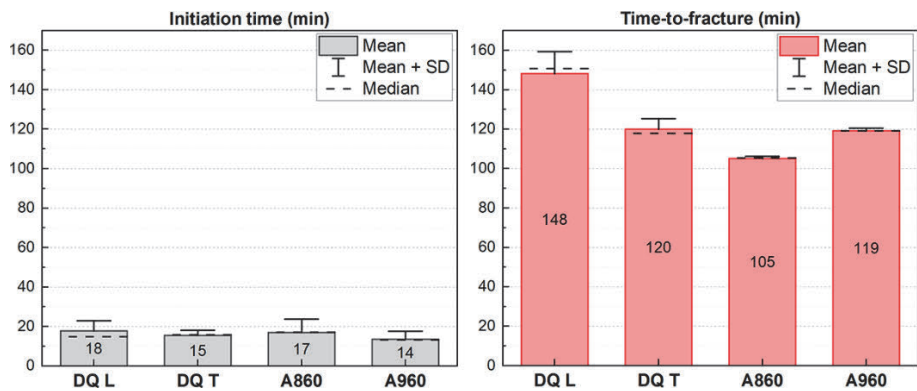


Fig. 26. t_i and t_f results of investigated materials stressed at 1000 MPa. (Reprinted, with permission, from Publication IV © 2022 Authors).

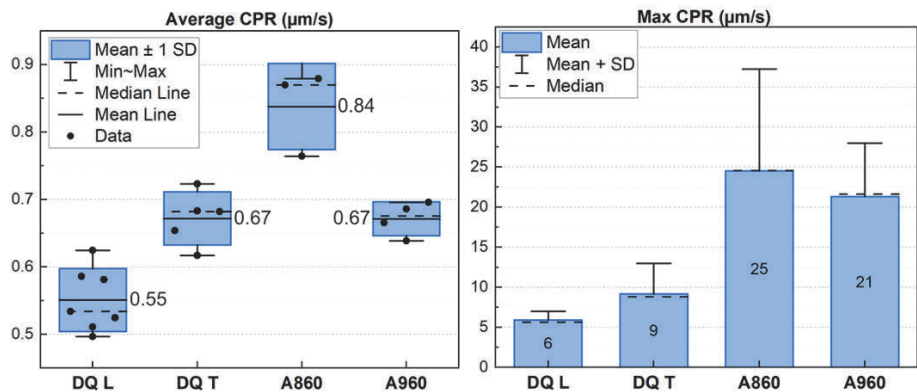


Fig. 27. Average CPR and maximum CPR results of investigated materials stressed at 1000 MPa. (Reprinted, with permission, from Publication IV © 2022 Authors).

If only equiaxed PAG structures are considered, the bigger PAG size of A960 leads to slower CPR, which suggests better performance. Differences in CPR can be affected by hydrogen diffusion and trapping properties as well as crack propagation mechanics.

For DQ L and T, differences cannot be explained by hydrogen diffusion since it is the same material. The main difference is therefore the PAG structure and its alignment to the crack plane. PAG elongation leads to a smaller average d_G for DQ L with more grain boundaries to traverse on the crack path as presented in Fig. 28. These factors most likely decelerate the CPR of DQ L, meaning that the direction of crack propagation in elongated PAG structure plays a role in HE resistance. The same observation was previously made for the same steel in Publication III with unnotched specimens.

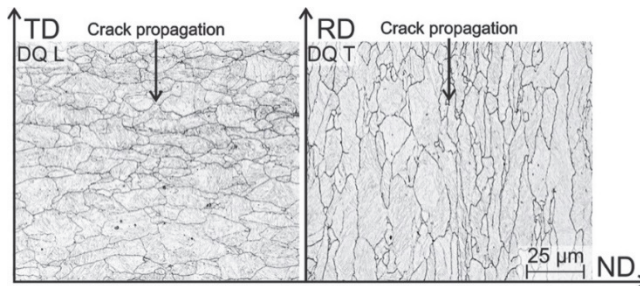


Fig. 28. PAG structure of crack planes of differently oriented DQ specimens. (Reprinted, with permission, from Publication IV © 2022 Authors).

The results indicate that the thermomechanical rolling process integrated with direct quenching can be a good choice for manufacturing steels with better HE resistance when elongated PAG structure is produced. A higher RD/ND ratio might improve the resistance even further if crack propagation is transverse to RD. However, more investigations are required since higher RD/ND ratio will also lead to bigger directional differences (L vs. T specimens), which can deteriorate the HE resistance if crack propagation is parallel to RD.

Examination of fracture surfaces shows that there is a ductile fracture area in the middle of the specimen, which is most likely responsible for the abrupt fracture in some of the tests. A macroscopic fracture surface with detailed microscopic views of the ductile middle region and the end of crack propagation is presented in Fig. 29. Crack propagation ends with a ductile area, and the ligament was broken by hand after testing.

Microscopic inspection of fracture surfaces (Fig. 30) reveals different PAG shape-dependent hydrogen-induced cracking mechanisms. The results are in accordance with Publication III, where elongated PAG structure led to transgranular quasi-cleavage crack propagation and equiaxed PAG structure showed a partly intergranular fracture.

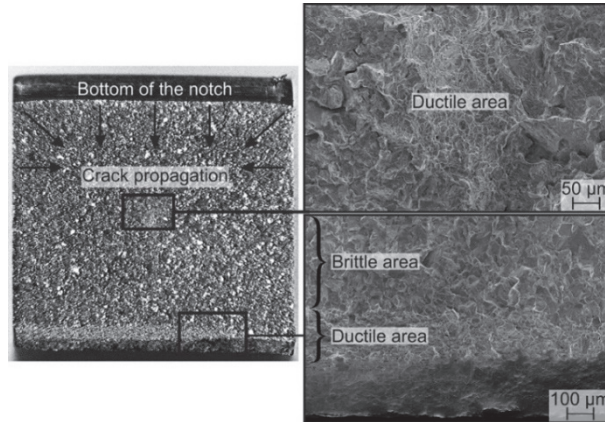


Fig. 29. Macroscopic view of whole fracture surface with highlighted microscopic views. (Reprinted, with permission, from Publication IV © 2022 Authors).

Same as unnotched specimens in Publication III, the fracture surface of notched DQ steel has a transgranular quasi-cleavage crack propagation mechanism. Because of the elongated and asymmetrical PAG structure of DQ, intergranular cracking is difficult to identify since it does not appear in a favourable manner. However, DQ T has indications of some intergranular cracking due to the flat features resembling separated grain boundary surfaces. Based on the size, shape, and topography of the observed flat features, they could be exposed grain boundaries. For equiaxed structures, intergranular features are easily recognized with a clear three-dimensional character of separated grain boundary surfaces and faceted morphology, as can be seen in the case of A860 and A960 steels. The intergranular fracture mechanism explains the faster CPR of re-austenitized steels and for DQ T, faster CPR results from a combination of some intergranular crack propagation with less grain boundaries on the crack path. According to the hydrogen-enhanced-plasticity mediated decohesion mechanism, grain boundaries are weakened by the presence of hydrogen and further enhanced hydrogen accumulation is provided by dislocation activity. If slip systems intersect PAGs, it

causes intergranular fracture (A860/A960), and intersecting with blocks/laths leads to quasi-cleavage fracture (DQ). The mechanism type depends on where local stress accentuation and hydrogen accumulation are attained first [38]. In this case, DQ has more dislocations, but more investigations are needed to quantify their effect.

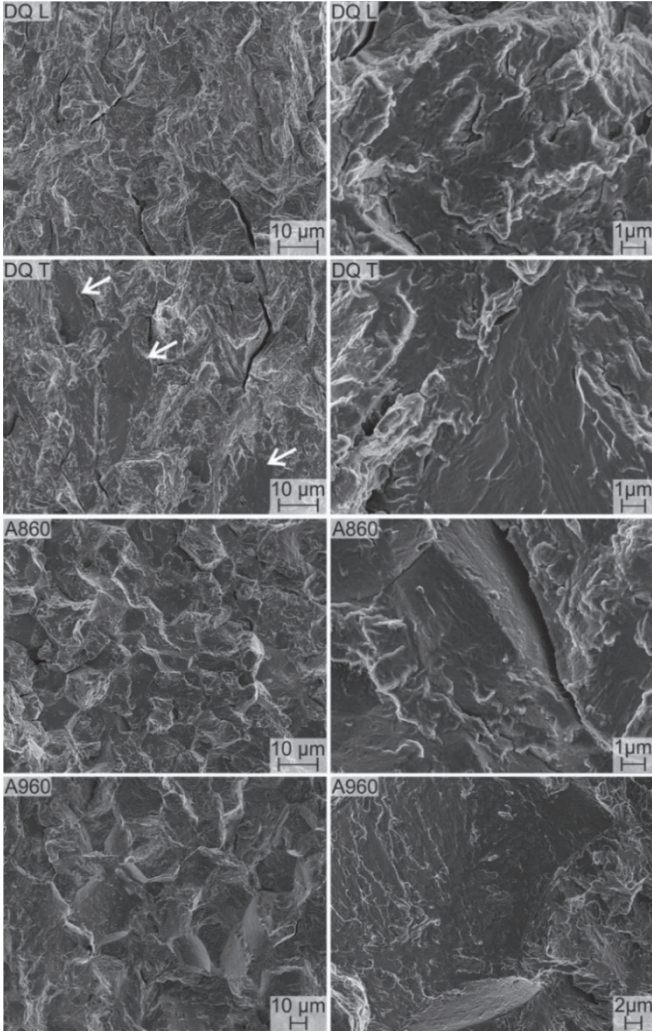


Fig. 30. Fracture surfaces of investigated steel grades with general (left column) and detailed views (right column) with white arrows marking the suspected intergranular features of DQ T. (Reprinted, with permission, from Publication IV © 2022 Authors).

In QT martensitic steels, hydrogen-induced cracks often initiate and propagate along the PAG boundaries [7], [46], [74]–[77]. Intergranular crack propagation can result from grain boundary embrittling impurity elements or the presence of second phase particles along the grain boundaries [78]. According to the literature, it is still controversial whether grain refinement is beneficial in hydrogen-induced delayed fracture of high-strength steels [46], [79]–[81]. There are indications of both smaller and larger PAG sizes being beneficial in HE resistance, but also results of PAG size not affecting HE susceptibility [82]. However, grain refinement does increase the grain boundary area, which reduces the concentration of the grain boundary embrittling impurity elements. In QT steels, grain refinement has proven to improve resistance against delayed fracture [46], [83], [84]. In medium-carbon martensitic steels, PAG refinement has been reported to be beneficial in hydrogen-induced cracking, which is explained by higher hydrogen absorption capacity [83]. In 8Ni-0.1C martensitic steel, grain refinement reduced the area fraction of intergranular fracture surfaces, which improved HE resistance [84]. According to others, a larger PAG size improves resistance to hydrogen-induced fracture due to higher threshold stress intensity and slower crack propagation [76], [81], [85].

In the case of A860 and A960, the increased S_V of A860 does not improve steel performance but leads to faster crack propagation. When t-F curves are compared, A860 has a slightly lower force value in comparison to the other steels. That could affect the final comparison of the equiaxed structures considering their CPR. The different initial force is distinctly grouped for A860; therefore, it is not a statistical error but is most likely related to the microstructure. A better comparison could be achieved by applying the same force, e.g., 75 N, instead of using the same arm distance. More investigations are required to confirm the CPR trend for the equiaxed structure. For example, a comparison of intermediate PAG size, e.g., 25 μm , with the utilization of the defined force would provide the necessary information.

In Publication III – IV, the same test material DQ steel shows an enhanced performance in comparison to other steels with less elongated or equiaxed PAG structures. In Publication III, the intergranular crack propagation was observed with an equiaxed PAG structure, but it could not be directly linked to the PAG shape because of the differences in alloying and manufacturing methods. The situation is different in Publication IV due to the same alloying, which provides the supporting evidence to the fact that equiaxed PAG structure is more prone to intergranular crack propagation. With equiaxed PAGs in the range of 10 – 40 μm , crack propagation is partly intergranular, which enhances crack propagation in hydrogen-

induced fracture. With the elongated PAG structure and average PAG size of 7.5 μm , crack propagation is transgranular quasi-cleavage, which results in the slowest crack propagation. It has been reported that delayed fracture of a steel hot-rolled in the recrystallization region is typically intergranular. When rolling is conducted in partial recrystallization or the unrecrystallization region, the delayed fracture is partly quasi-cleavage and quasi-cleavage, respectively, which is observed here also with DQ [74].

In studies regarding ausformed and tempformed steels, HE has been mitigated with elongated PAG structure. The proposed reason for better HE resistance is transgranular quasi-cleavage crack propagation and high delayed fracture resistance [7], [74], [75], [77], [80]. Utilization of additional rapid heating and tempering treatment has been proven to change the crack path further from quasi-cleavage to ductile fracture through cementite refinement [23], [86]. In comparison to QT steel with an equiaxed PAG structure, ultrafine elongated PAG boundaries have much larger dihedral angle in the transverse direction. Therefore, intergranular crack propagation requires more deflection in the elongated structure. The energy required for intergranular cracking increases with the number and degree of such deflections, which explains why equiaxed structure is more prone to intergranular fracture [7]. Based on the elongated PAG structure, DQ steel should have similar HE resistance as ausformed or tempformed steels. The obtained results support this as PAG shape correlates with the crack propagation mechanism, and elongated shape favours transgranular and equiaxed shape intergranular fracture.

4.2.3 Interrupted tuning-fork tests

For DQ T, interrupted tests are conducted with various charging times to study crack initiation and propagation mechanisms. The obtained t-F curves paired with a side view of a cracked specimen and corresponding macroscopic images of the fracture surface are presented in Fig. 31. The discoloured area represents the propagated crack, and it looks like crack propagation occurs slightly faster from the corners of the specimens. Therefore, the ductile region in the middle of the fracture surface (see Fig. 29) is most likely a consequence of crack coalescence since crack propagation occurs in three different directions. In an equiaxed PAG structure, the crack coalescence leads to an enhancement of crack growth that is seen as an abrupt drop in F values around 100 – 120 min (see Fig. 25). The abrupt fracture elevates the maximum CPR to a 2 – 3 times higher level in comparison to

that of DQ steel. The crack growth rate enhancement differences suggest that the equiaxed PAG structure is more sensitive to sudden fractures caused by hydrogen.

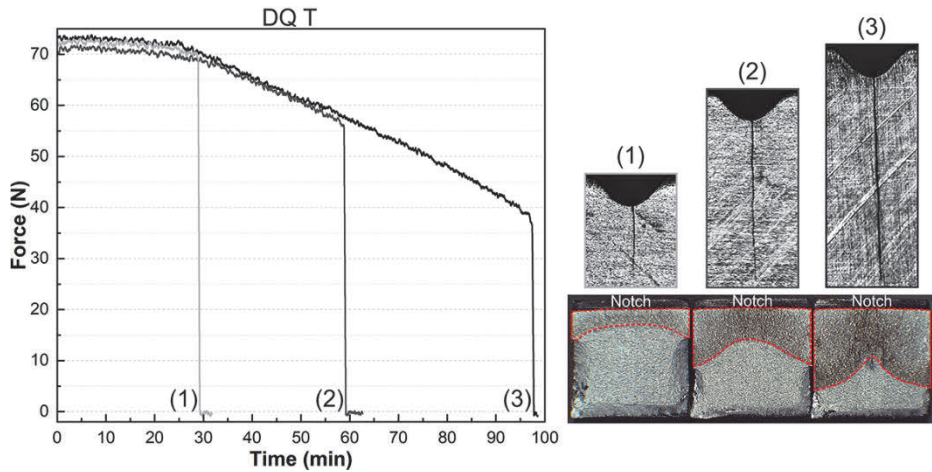


Fig. 31. Interrupted tests. (Reprinted, with permission, from Publication IV © 2022 Authors).

Separate interrupted tests, which were terminated after approximately 5 – 10 N drop in the force values, are conducted for all test materials. In these interrupted tests, initiated cracks were investigated with a laser microscope (etched PAGs), and EBSD analysis (IPF), as presented in Fig. 32.

The observations are like the ones made with fracture surface analysis. DQ steel has straight transgranular crack propagation, and A860 and A960 steels manifest a mixture of transgranular and intergranular crack propagation with pronounced branching features. In all cases, cracks most likely initiate at the grain boundaries and further crack propagation is transgranular. However, in the equiaxed PAG structure, the crack path quickly changes to partly intergranular fracture, but it continues as transgranular in the elongated structure.

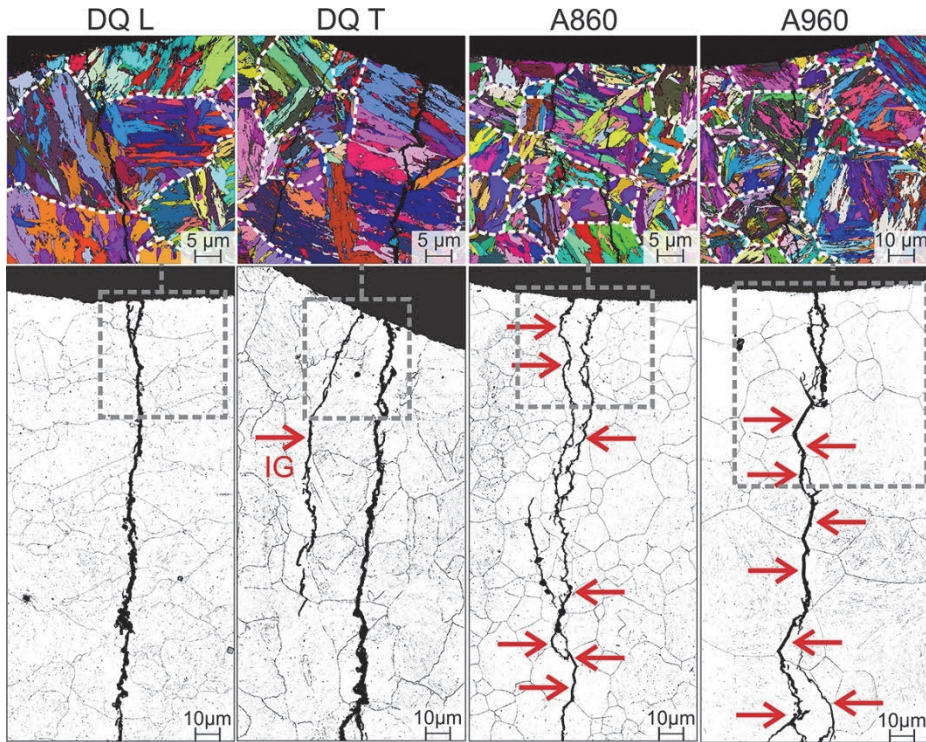


Fig. 32. Crack initiation and propagation at the tip of the notch. Intergranular (IG) crack propagation is marked with red arrows. (Reprinted, with permission, from Publication IV © 2022 Authors).

4.3 Hydrogen permeation

Hydrogen permeation tests are used to investigate hydrogen diffusion and trapping properties of Armco iron, DQ, A860, and A960. The obtained decay and build-up transients of Armco, DQ, A860, and A960 with fitted curves are presented in Fig. 33. The transients are reproducible and used to calculate the D and C_H of each material. The experimental and fitted curves overlap with a good fit, which indicates that the permeation of hydrogen is diffusion-controlled [64]. The calculated D values are presented in Fig. 34, showing that from the studied steels, DQ has the slowest hydrogen diffusivity in comparison to re-austenitized steels. As expected, the reference material, Armco iron, has significantly faster diffusivity due to its softer ferritic microstructure. Armco iron has been widely studied and

therefore selected as the reference material. The average D of Armco is $3.4 \times 10^{-5} \text{ cm}^2/\text{s}$, which is in the same order of magnitude when compared to similar tests and therefore verifies the reliability of the permeation data [64], [87]. Studied steels also have diffusion coefficients that are in the range of the values obtained from the literature ($\sim 1 \times 10^{-6}$ to $8 \times 10^{-7} \text{ cm}^2/\text{s}$) for predominantly martensitic steels with similar mechanical properties [36], [69].

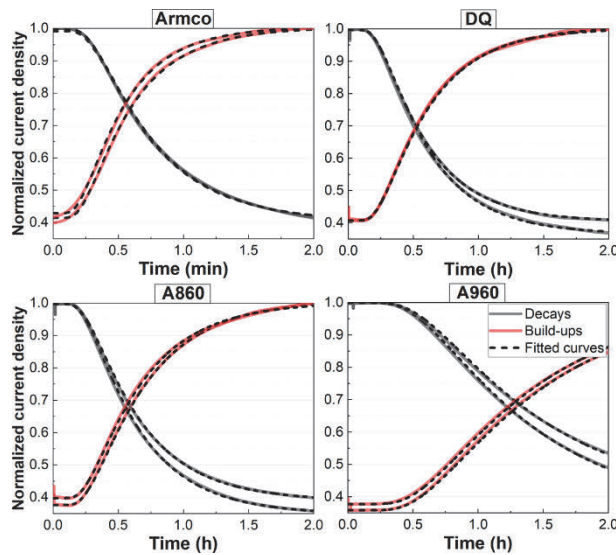


Fig. 33. Transient curves with fittings of Armco, DQ, A860, and A960. Notice the different time scales. (Reprinted, with permission, from Publication IV © 2022 Authors).

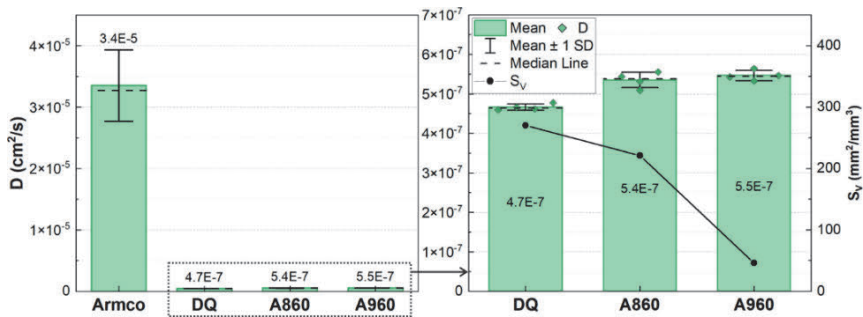


Fig. 34. Diffusion coefficients of Armco, DQ, A860, and A960 with S_v correlation. (Reprinted, with permission, from Publication IV © 2022 Authors).

Typically, increasing mechanical strength leads to a decrease in the hydrogen diffusion coefficient. In this case, mechanical properties such as tensile strength and hardness are relatively similar. DQ steel, however, has a higher YS in comparison to A860 and A960, which suggests that it has a higher dislocation density. Also, EBSD analysis showed a slightly higher fraction of the low-angle boundaries. Consequently, the hydrogen trap density should be higher for DQ steel.

The slower hydrogen diffusivity of DQ steel is attributed to the manufacturing method, which produces higher fraction of lath boundaries and higher dislocation density, which all contribute to the trapping of hydrogen and therefore retard the hydrogen diffusion. There is no correlation between D and the PAG structure or S_V . DQ steel and A860 have similar S_V but different D , and A860 and A960 have a fourfold difference in S_V but similar D . Therefore, PAG boundaries are not the predominant diffusion paths but traps in the studied steels, and other interfaces (packet, block, lath boundaries) have a greater effect on hydrogen diffusion.

Although there is no correlation between S_V and D , CPR results follow the same pattern as D . The slowest D and CPR are both observed with DQ steel, and faster CPR, as well as hydrogen diffusivity, are linked to A860 and A960 steels. Faster fracture of A860 and A960 can be a result of both intergranular crack propagation and faster hydrogen diffusivity.

The density of reversible/weak traps is evaluated with the surface area difference (A) of the total discharge transient and a theoretical decay curve fitted with previously determined average D . Fig. 35 presents the obtained A and calculated N_T .

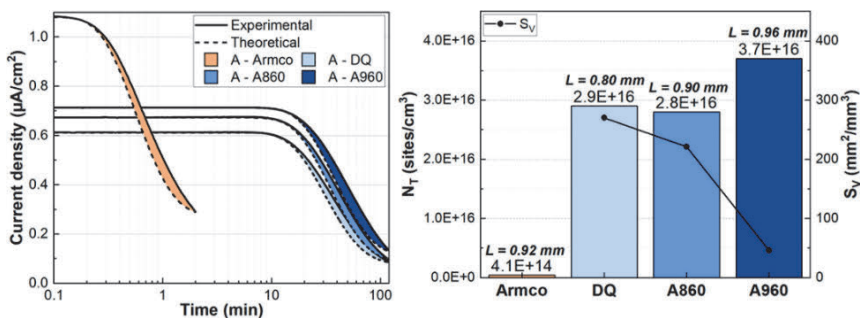


Fig. 35. Area difference of experimental and theoretical decay curve and calculated N_T with S_V correlation. (Reprinted, with permission, from Publication IV © 2022 Authors).

In accordance with the theory, Armco iron has a few orders smaller N_T in comparison to steels. At the beginning of this research, the assumption was that lower S_V would lead to a lower amount of hydrogen traps. But in fact, the density of weak traps is the opposite of that with A960 having elevated trap density. In this case, smaller S_V leads to higher N_T , which indicates that PAG boundaries are acting as strong traps. The higher N_T of A960 can then be attributed to the larger surface area of the steel matrix with other trapping sites.

However, the significance of these results is debatable since the obtained N_T differences are small. More investigations are required to quantify the density of reversible and irreversible traps. There are different ways to study the density of irreversible traps. It can be done e.g. with TDS or by conducting several permeation and desorption curves and analysing their surface area differences [88]–[90]. However, it can be challenging to maintain an unoxidized surface on the charging side of the membrane. Between the permeation curves, the hydrogen charging cell needs to be emptied quickly while protecting the steel surface from oxidation. One option is to use a Pd coating on both sides, which would protect the specimen but would also create a diffusion barrier similar to the oxide layer.

5 Summary and conclusions

The main goals of this thesis were the development of the novel tuning-fork test and its utilization to understand the effect of PAG structure of ultrahigh-strength steels on hydrogen embrittlement susceptibility.

5.1 Tuning-fork testing

The tuning-fork test was aimed to be a relatively simple but fast testing system, which would not require tensile test equipment. Over the course of this thesis, the test method was developed to the stage where it fulfilled all the above-mentioned requirements, and it could be successfully used in the ranking and comparison of the hydrogen embrittlement susceptibility of different ultrahigh-strength steels (450 – 600 HBW). With the current testing system, a test conducted with a notched specimen geometry and a loadcell clamping can provide the following information in a matter of hours:

- Initiation time
- Crack propagation time
- Time-to-fracture
- Average and maximum crack propagation rate (CPR)

After the tests, fractography will provide more information regarding the crack paths and propagation mechanisms. Interrupted testing allows a more precise study of crack initiation and first stages of crack propagation. The testing method has good repeatability, and it can be used to compare similar microstructures of ultrahigh-strength steels. Overall, the tuning-fork test provides a variety of parameters that are important in understanding hydrogen-induced cracking susceptibility.

5.2 PAG structure

The effect of PAG shape and size was studied with tuning-fork tests using two DQ steels with different elongated microstructures and RQ steel with an equiaxed PAG structure. The comparison was conducted also for DQ steel that was re-austenitized and quenched to produce equiaxed PAG structures with different grain sizes from

the same alloy composition complemented with traditional permeation tests. Based on the results, the following conclusions and summary can be made:

- Elongated PAG morphology with microstructural anisotropy produces different results depending on the crack propagation direction. Best results or slowest CPR is achieved when the crack propagation is transverse to the rolling direction (RD). Crack propagation is faster parallel to the RD. For RQ steel with an equiaxed PAG structure, there are no significant differences between differently oriented specimens. Therefore, the structural design of the application that utilizes DQ steels in hydrogen-containing environments should consider the possible crack propagation direction of hydrogen-induced cracking.
- Crack propagation types are different depending on the PAG shape. For all PAG morphologies, crack most likely initiates at a grain boundary and propagation continues first as transgranular. However, for the equiaxed PAG structure, the mechanism shifts to partly intergranular fracture. In the case of elongated PAG structure, crack propagation is mostly transgranular quasi-cleavage, but there are some indications of intergranular crack propagation visible as flat features on the fracture surface when the crack propagates parallel to the RD. Different types of crack propagation are associated with the microstructural alignment and the geometrical shape of the PAG structure.
- With the same alloying and average PAG size, the transgranular quasi-cleavage crack propagation of elongated PAG structure leads to a significantly slower CPR in comparison to that of the equiaxed PAG structure with intergranular crack propagation. The same observation is made for PAG comparison with different alloying. Therefore, an elongated PAG structure is considered to enhance hydrogen embrittlement resistance.
- With the same alloying, the hydrogen diffusion coefficient (D) is lowest for DQ steel with elongated PAG structure and equally higher for equiaxed structures independent of the PAG size. Slower CPR can be linked to lower D . No correlation is observed between D and PAG boundary surface area (S_V), indicating that PAG boundaries are not the predominant diffusion paths. With increasing PAG size or the smaller S_V , the density of reversible trapping sites increases. Therefore, PAG boundaries may act as strong hydrogen traps in the investigated steel grades.

6 Novel features

To the best knowledge of the author, these observations are considered novel at the time of publishing:

- Novel tuning-fork test, which was developed as a tool to study the hydrogen-induced cracking of ultrahigh-strength steels which includes all stages of development such as geometry, cells, different clamping systems, and different testing procedures (until fracture/interrupted tests) as well as result analysis with a specially developed graphical user interface tool (Freader).
- The utilized materials comparison that allowed investigation of different PAG shapes/sizes with the same alloying composition, microstructure, tensile, and hardness properties.
- The effect of PAG shapes on the crack propagation mechanism and crack propagation rate.
- Hydrogen permeation test set-up including glass cell geometry, sealing, and clamping was designed and built by the author to complement the tuning-fork tests. Therefore, the permeation cell is one of a kind and it has a unique graphical user interface tool (Permeator) specifically developed for the result analysis of the hydrogen permeation experiments.

7 Future research

The development of the tuning-fork test will be continued, and there are several ideas on how to improve and broaden its utilization. The first important step will be to compare and verify the obtained data with some traditional testing methods such as CL or SSRT. The comparison should be conducted preferably with notched specimens and in a similar hydrogen charging environment.

In its current form, the main disadvantage of the tuning-fork test is the incapability to compare different stress levels. More development work is required to address this matter since it restricts a broader comparison of different materials. The lower stress levels have poor repeatability, which causes deviation of results, but this may be improved by adjustments to the hydrogen charging environment and notch modifications, e.g., by decreasing the stress concentration factor. There is also an option of stressing the specimens so that there is a small plastic zone, which would allow different types of studies.

Currently, the testing method is limited to the testing of ultrahigh-strength steels, but it could potentially be utilized in testing of other materials as well. It would likely require some modifications of the geometry and testing environment, but in theory, studying, e.g., stress corrosion cracking of stainless steel is a viable possibility. The tuning-fork test can also be used as a simple immersion test, but it provides more information regarding the cracking mechanisms due to the loadcell.

One idea is also to perform interrupted testing so that the specimen is taken out of the cell after the crack has initiated and kept in air to see if crack propagation continues. The specimen could be taken out of the cell after the crack has propagated, e.g., 25% or 50%, to see what the critical crack length is for crack propagation to continue. This would reflect on delayed cracking susceptibility and those production processes where hydrogen is only present in cycles.

In terms of the PAG structure, it would be important to correlate the degree of PAG elongation with hydrogen embrittlement susceptibility. Is it possible to achieve better results with a more elongated PAG structure, or does it emphasise the directional differences and therefore deteriorate hydrogen susceptibility? There is also a remaining question of different grain sizes of the equiaxed structure and investigation of some intermediate grain sizes between 10 and 40 μm is recommended. The inferior results of the equiaxed PAG structure were linked to the intergranular crack propagation, but is it possible to suppress the intergranular crack propagation by additional low-temperature tempering treatment? If so, would the same tempering treatment further improve the direct-quenched steels? Direct

quenching is more cost-efficient without tempering. However, if additional tempering would drastically improve the hydrogen embrittlement resistance, could it be used to manufacture ultrahigh-strength steels with superior hydrogen embrittlement resistance? Finally, the results indicated that PAG boundaries act as strong hydrogen trapping sites, which needs further quantification. A similar comparison of the present microstructures can be completed with the permeation experiments that determine the density of irreversible trapping sites which would confirm our current observations.

List of references

- [1] W. H. Johnson, "II. On some remarkable changes produced in iron and steel by the action of hydrogen and acids," *Proc. R. Soc. London*, vol. 23, no. 156–163, pp. 168–179, Dec. 1875.
- [2] H. K. D. H. Bhadeshia, "Prevention of hydrogen embrittlement in steels," *ISIJ Int.*, vol. 56, no. 1, pp. 24–36, Jan. 2016.
- [3] J. Venezuela, Q. Liu, M. Zhang, Q. Zhou, and A. Atrens, "A review of hydrogen embrittlement of martensitic advanced high-strength steels," *Corros. Rev.*, vol. 34, no. 3, pp. 153–186, Jun. 2016.
- [4] J. Kömi, P. Karjalainen, and D. Porter, "Direct-Quenched Structural Steels," in *Encyclopedia of Iron, Steel, and Their Alloys*, CRC Press, 2016, pp. 1109–1125.
- [5] S. Satyapal, "Hydrogen: A Clean, Flexible Energy Carrier," *Energy Efficiency & Renewable Energy*, 21-Feb-2017. [Online]. Available: <https://www.energy.gov/eere/articles/hydrogen-clean-flexible-energy-carrier>. [Accessed: 18-Jun-2022].
- [6] C. J. McMahon, "Hydrogen-induced intergranular fracture of steels," *Eng. Fract. Mech.*, vol. 68, no. 6, pp. 773–788, Apr. 2001.
- [7] Y. Nie, Y. Kimura, T. Inoue, F. Yin, E. Akiyama, and K. Tsuzaki, "Hydrogen Embrittlement of a 1500-MPa Tensile Strength Level Steel with an Ultrafine Elongated Grain Structure," *Metall. Mater. Trans. A*, vol. 43, no. 5, pp. 1670–1687, May 2012.
- [8] WorldAutoSteel, "Advanced High-Strength Steel (AHSS) Definitions," 2022. [Online]. Available: <https://www.worldautosteel.org/steel-basics/automotive-advanced-high-strength-steel-ahss-definitions/>. [Accessed: 18-Jun-2022].
- [9] T. V Philip and T. J. McCaffrey, "Ultrahigh-Strength Steels," in *Properties and Selection: Irons, Steels, and High-Performance Alloys*, vol. 1, ASM International, 1990, pp. 430–448.
- [10] SSAB, "Ultra-High Strength Steels (UHSS): what are they and how they improve vehicles," 2022. [Online]. Available: <https://www.ssab.com/en/brands-and-products/docol/ultra-high-strength-steel>. [Accessed: 22-Jun-2018].
- [11] W. D. Callister and D. G. Rethwisch, *Materials science and engineering: An Introduction*, 9th ed. Hoboken, New Jersey: John Wiley & Sons, Inc., 2011.
- [12] H. Bhadeshia and R. Honeycombe, *Steels Microstructure and Properties*, 3rd ed. Oxford, United Kingdom: Elsevier, 2006.
- [13] G. Krauss, "Deformation and fracture in martensitic carbon steels tempered at low temperatures," *Metall. Mater. Trans. B*, vol. 32, no. 2, pp. 205–221, Apr. 2001.
- [14] G. Krauss, "Quench and Tempered Martensitic Steels: Microstructures and

- Perfromance,” in *Comprehensive Materials Processing*, vol. 12, Elsevier, 2014, pp. 363–378.
- [15] G. Krauss, “Martensite in steel: strength and structure,” *Mater. Sci. Eng. A*, vol. 273–275, pp. 40–57, Dec. 1999.
- [16] B. Hutchinson *et al.*, “Microstructures and hardness of as-quenched martensites (0.1–0.5%C),” *Acta Mater.*, vol. 59, no. 14, pp. 5845–5858, Aug. 2011.
- [17] Y. Momotani, A. Shibata, T. Yonemura, Y. Bai, and N. Tsuji, “Effect of initial dislocation density on hydrogen accumulation behavior in martensitic steel,” *Scr. Mater.*, vol. 178, pp. 318–323, Mar. 2020.
- [18] S. Morito, Y. Adachi, and T. Ohba, “Morphology and Crystallography of Sub-Blocks in Ultra-Low Carbon Lath Martensite Steel,” *Mater. Trans.*, vol. 50, no. 8, pp. 1919–1923, Jun. 2009.
- [19] A. Shibata, T. Murata, H. Takahashi, T. Matsuoka, and N. Tsuji, “Characterization of Hydrogen-Related Fracture Behavior in As-Quenched Low-Carbon Martensitic Steel and Tempered Medium-Carbon Martensitic Steel,” *Metall. Mater. Trans. A*, vol. 46, no. 12, pp. 5685–5696, Dec. 2015.
- [20] G. Krauss, “Martensitic Structure,” in *Encyclopedia of Iron, Steel, and Their Alloys*, CRC Press, 2016, pp. 2182–2187.
- [21] A. Saastamoinen, A. Kaijalainen, T. T. Nyo, P. Suikkanen, D. Porter, and J. Kömi, “Direct-quenched and tempered low-C high-strength structural steel: The role of chemical composition on microstructure and mechanical properties,” *Mater. Sci. Eng. A*, vol. 760, no. April, pp. 346–358, Jul. 2019.
- [22] A. Kaijalainen, “Effect of microstructure on the mechanical properties and bendability of direct-quenched ultrahigh-strength steels,” *Acta Universitatis Ouluensis C582*, Oulu, Finland, 2016.
- [23] A. Nagao, T. Ito, and T. Obinata, “Development of YP 960 and 1100 MPa class ultra high strength steel plates with excellent toughness and high resistance to delayed fracture for construction and industrial machinery,” *JFE Tech. Rep.*, no. 11, pp. 13–18, Jun. 2008.
- [24] K. Nishioka and K. Ichikawa, “Progress in thermomechanical control of steel plates and their commercialization,” *Sci. Technol. Adv. Mater.*, vol. 13, no. 2, p. 023001, Apr. 2012.
- [25] Y. H. Bae, J. S. Lee, J.-K. Choi, W.-Y. Choo, and S. H. Hong, “Effects of Austenite Conditioning on Austenite/Ferrite Phase Transformation of HSLA Steel,” *Mater. Trans.*, vol. 45, no. 1, pp. 137–142, Nov. 2004.
- [26] J. Woodtli and R. Kieselbach, “Damage due to hydrogen embrittlement and stress corrosion cracking,” *Eng. Fail. Anal.*, vol. 7, no. 6, pp. 427–450, Dec. 2000.
- [27] S. K. Dwivedi and M. Vishwakarma, “Hydrogen embrittlement in different materials: A review,” *Int. J. Hydrogen Energy*, vol. 43, no. 46, pp. 21603–21616, Nov. 2018.
- [28] S. Ramamurthy and A. Atrens, “Stress corrosion cracking of high-strength

- steels,” *Corros. Rev.*, vol. 31, no. 1, pp. 1–31, Mar. 2013.
- [29] J. Ćwiek, “Hydrogen degradation of high-strength steels,” *J. Achiev. Mater. Manuf. Eng.*, vol. 37, no. 2, pp. 193–212, Dec. 2009.
- [30] H. G. Nelson, “Hydrogen Embrittlement,” in *Treatise on Materials Science and Technology*, vol. 25, C. L. Briant and S. K. Banerji, Eds. Elsevier, 1983, pp. 275–359.
- [31] D. Rudomilova, T. Prošek, and G. Luckeneder, “Techniques for investigation of hydrogen embrittlement of advanced high strength steels,” *Corros. Rev.*, vol. 36, no. 5, pp. 413–434, Sep. 2018.
- [32] ACM International, *Corrosion: Environments and Industries*, vol. 13C. Materials Park, OH: ASM International, 2006.
- [33] D. Rudomilova *et al.*, “The effect of microstructure on hydrogen permeability of high strength steels,” *Mater. Corros.*, vol. 71, no. 6, pp. 909–917, Jun. 2020.
- [34] Q. Liu, Q. Zhou, J. Venezuela, M. Zhang, J. Wang, and A. Atrens, “A review of the influence of hydrogen on the mechanical properties of DP, TRIP, and TWIP advanced high-strength steels for auto construction,” *Corros. Rev.*, vol. 34, no. 3, pp. 127–152, Jun. 2016.
- [35] M. B. Djukic, G. M. Bakic, V. Sijacki Zeravcic, A. Sedmak, and B. Rajcic, “The synergistic action and interplay of hydrogen embrittlement mechanisms in steels and iron: Localized plasticity and decohesion,” *Eng. Fract. Mech.*, vol. 216, no. May, p. 106528, 2019.
- [36] J. Venezuela, Q. Zhou, Q. Liu, M. Zhang, and A. Atrens, “Hydrogen Trapping in Some Automotive Martensitic Advanced High-Strength Steels,” *Adv. Eng. Mater.*, vol. 20, no. 1, p. 1700468, Jan. 2018.
- [37] R. Silverstein, D. Eliezer, and E. Tal-Gutelmacher, “Hydrogen trapping in alloys studied by thermal desorption spectrometry,” *J. Alloys Compd.*, vol. 747, pp. 511–522, May 2018.
- [38] A. Nagao, M. Dadfarnia, B. P. Somerday, P. Sofronis, and R. O. Ritchie, “Hydrogen-enhanced-plasticity mediated decohesion for hydrogen-induced intergranular and ‘quasi-cleavage’ fracture of lath martensitic steels,” *J. Mech. Phys. Solids*, vol. 112, pp. 403–430, 2018.
- [39] T. Depover, A. Laureys, D. Pérez Escobar, E. Van den Eeckhout, E. Wallaert, and K. Verbeken, “Understanding the Interaction between a Steel Microstructure and Hydrogen,” *Materials (Basel)*, vol. 11, no. 5, p. 698, Apr. 2018.
- [40] X. Li, X. Ma, J. Zhang, E. Akiyama, Y. Wang, and X. Song, “Review of Hydrogen Embrittlement in Metals: Hydrogen Diffusion, Hydrogen Characterization, Hydrogen Embrittlement Mechanism and Prevention,” *Acta Metall. Sin. (English Lett.)*, vol. 33, no. 6, pp. 759–773, 2020.
- [41] B. Sun, D. Wang, X. Lu, D. Wan, D. Ponge, and X. Zhang, “Current Challenges and Opportunities Toward Understanding Hydrogen Embrittlement Mechanisms in Advanced High-Strength Steels: A Review,”

- Acta Metall. Sin. English Lett.*, vol. 34, no. 6, pp. 741–754, Jun. 2021.
- [42] R. W. Hertzberg, R. P. Vinci, and J. L. Hertzberg, *Deformation and Fracture Mechanics of Engineering Materials*, 5th ed. Hoboken, NJ: John Wiley & Sons, Inc., 2012.
- [43] J. L. González-Velázquez, *Fractography and Failure Analysis*, vol. 3. Cham, Switzerland: Springer, 2018.
- [44] L. Cho *et al.*, “Characteristics and mechanisms of hydrogen-induced quasi-cleavage fracture of lath martensitic steel,” *Acta Mater.*, vol. 206, p. 116635, Mar. 2021.
- [45] M. L. Martin, J. A. Fenske, G. S. Liu, P. Sofronis, and I. M. Robertson, “On the formation and nature of quasi-cleavage fracture surfaces in hydrogen embrittled steels,” *Acta Mater.*, vol. 59, no. 4, pp. 1601–1606, Feb. 2011.
- [46] Y. Kimura, S. Takagi, T. Hara, S. Terasaki, and K. Tsuzaki, “Hydrogen-induced delayed fracture of a martensitic steel with fine prior-austenite grain size,” *J. Phys. IV*, vol. 112, pp. 403–406, Oct. 2003.
- [47] A. Turnbull, “Test methods for environment assisted cracking,” *Br. Corros. J.*, vol. 27, no. 4, pp. 271–289, Jul. 1992.
- [48] T. Depover, D. Wan, D. Wang, A. Barnoush, and K. Verbeken, “The effect of hydrogen on the crack initiation site of TRIP-assisted steels during in-situ hydrogen plasma micro-tensile testing: Leading to an improved ductility?,” *Mater. Charact.*, vol. 167, no. July, p. 110493, Sep. 2020.
- [49] J. Venezuela *et al.*, “Equivalent hydrogen fugacity during electrochemical charging of some martensitic advanced high-strength steels,” *Corros. Sci.*, vol. 127, no. March, pp. 45–58, Oct. 2017.
- [50] M. Ichiba, K. Takai, and J. Sakai, “Effects of Test Conditions on Corrosion Reactions and Hydrogen Absorption in Hydrogen Embrittlement Tests Using an Ammonium Thiocyanate Solution,” *ISIJ Int.*, vol. 56, no. 3, pp. 397–404, Mar. 2016.
- [51] J. Rehr, K. Mraczek, A. Pichler, and E. Werner, “Mechanical properties and fracture behavior of hydrogen charged AHSS/UHSS grades at high- and low strain rate tests,” *Mater. Sci. Eng. A*, vol. 590, pp. 360–367, Jan. 2014.
- [52] S. Ramamurthy, W. M. L. Lau, and A. Atrens, “Influence of the applied stress rate on the stress corrosion cracking of 4340 and 3.5NiCrMoV steels under conditions of cathodic hydrogen charging,” *Corros. Sci.*, vol. 53, no. 7, pp. 2419–2429, Jul. 2011.
- [53] A. Chernyaev, “Development of a rapid stress corrosion cracking test method for high-strength steels,” Aalto University School of Chemical Technology, Espoo, Finland, 2017.
- [54] *Standard Practice for Preparation and Use of Bent-Beam Stress-Corrosion Test Specimens*. ASTM G39 - 99, 1999.
- [55] *Corrosion of metals and alloys. Stress corrosion testing. Part 2: preparation and use of bend-beam specimen*. SFS-EN ISO 7539-2, 1989.

- [56] *Standard Practice for Making and Using C-Ring Stress-Corrosion Test Specimens*. ASTM G38 - 01, 2007.
- [57] *Standard Practice for Making and Using U-Bend Stress-Corrosion Test Specimens*. ASTM G30 - 97, 2009.
- [58] *Corrosion of metals and alloys - Stress corrosion testing. Part 3: Preparation and use of U-bend specimens*. SFS-EN ISO 7539-3, 1989.
- [59] *Corrosion of metals and alloys. Stress corrosion testing. Part 4: preparation and use of uniaxially loaded tension specimens*. SFS-EN ISO 7539-4, 1989.
- [60] *Testing the resistance of wrought aluminium alloys to stress corrosion cracking*. DIN 50908, 1993.
- [61] *Method of measurement of hydrogen permeation and determination of hydrogen uptake and transport in metals by an electrochemical technique*. SFS-EN ISO 17081, 2014.
- [62] *Standard Practice for Evaluation of Hydrogen Uptake, Permeation, and Transport in Metals by an Electrochemical Technique*. ASTM G148 - 97, 2003.
- [63] SPA Plating, “Spa Plating: Palladium Tank Plating Solution,” 2017. [Online]. Available: <https://www.goldn.co.uk/product/palladium-tank-plating-solution/>. [Accessed: 22-Jun-2018].
- [64] T. Zakroczymski, “Adaptation of the electrochemical permeation technique for studying entry, transport and trapping of hydrogen in metals,” *Electrochim. Acta*, vol. 51, no. 11, pp. 2261–2266, Feb. 2006.
- [65] D. Mallick, N. Mary, V. S. Raja, and B. Normand, “Study of Diffusible Behavior of Hydrogen in First Generation Advanced High Strength Steels,” *Metals (Basel)*, vol. 11, no. 5, p. 782, May 2021.
- [66] Q. Liu and A. Atrens, “Reversible hydrogen trapping in a 3.5NiCrMoV medium strength steel,” *Corros. Sci.*, vol. 96, pp. 112–120, Jul. 2015.
- [67] J. Venezuela, Q. Zhou, Q. Liu, M. Zhang, and A. Atrens, “Influence of hydrogen on the mechanical and fracture properties of some martensitic advanced high strength steels in simulated service conditions,” *Corros. Sci.*, vol. 111, pp. 602–624, Oct. 2016.
- [68] Q. Liu, J. Venezuela, M. Zhang, Q. Zhou, and A. Atrens, “Hydrogen trapping in some advanced high strength steels,” *Corros. Sci.*, vol. 111, pp. 770–785, Oct. 2016.
- [69] J. Venezuela *et al.*, “Hydrogen embrittlement of an automotive 1700 MPa martensitic advanced high-strength steel,” *Corros. Sci.*, vol. 171, p. 108726, Jul. 2020.
- [70] *Corrosion of metals and alloys. Stress corrosion testing. Part 1: General guidance on testing procedures*. SFS-EN ISO 7539-1, 2012.
- [71] M. Philippe, *Corrosion Mechanisms in Theory and Practice*, 2nd ed. New York: Marcel Dekker Ink, 2002.
- [72] G. Wranglen, “Pitting and sulphide inclusions in steel,” *Corros. Sci.*, vol.

- 14, no. 5, pp. 331–349, Jan. 1974.
- [73] Z. Szklarska-śmialowska and E. Lunarska, “The effect of sulfide inclusions on the susceptibility of steels to pitting, stress corrosion cracking and hydrogen embrittlement,” *Mater. Corros.*, vol. 32, no. 11, pp. 478–485, Nov. 1981.
- [74] S. Yamasaki, T. Tarui, and M. Kubota, “Evaluation method for delayed fracture susceptibility of steels and development of high tensile strength steels with high delayed fracture resistance,” *Nippon Steel Tech. Rep.*, no. 80, pp. 50–55, Jul. 1999.
- [75] Y. Kimura, T. Inoue, E. Akiyama, and K. Tsuzaki, “Hydrogen Embrittlement in Ultrafine Elongated Grain Structure Steel Processed by Warm Tempforming,” in *International Hydrogen Conference (IHC 2012): Hydrogen-Materials Interactions*, B. P. Somerday and P. Sofronis, Eds. ASME Press, 2014, pp. 101–110.
- [76] G. F. Li, R. G. Wu, and T. C. Lei, “Effect of prior austenitic grain size on stress corrosion cracking of a high-strength steel,” *Metall. Trans. A*, vol. 21, no. 1, pp. 503–505, Jan. 1990.
- [77] J. S. Kim, Y. H. Lee, D. L. Lee, K.-T. Park, and C. S. Lee, “Microstructural influences on hydrogen delayed fracture of high strength steels,” *Mater. Sci. Eng. A*, vol. 505, no. 1–2, pp. 105–110, Apr. 2009.
- [78] M. Nagumo and H. Matsuda, “Function of hydrogen in intergranular fracture of martensitic steels,” *Philos. Mag. A*, vol. 82, no. 17–18, pp. 3415–3425, Nov. 2002.
- [79] Y. Liu, M. Wang, and G. Liu, “Hydrogen trapping in high strength martensitic steel after austenitized at different temperatures,” *Int. J. Hydrogen Energy*, vol. 38, no. 33, pp. 14364–14368, Nov. 2013.
- [80] Y. Kimura, Y. Sakai, T. Hara, A. Belyakov, and K. Tsuzaki, “Hydrogen induced delayed fracture of ultrafine grained 0.6% O steel with dispersed oxide particles,” *Scr. Mater.*, vol. 49, no. 11, pp. 1111–1116, Dec. 2003.
- [81] J. F. Lessar and W. W. Gerberich, “Grain Size Effects in Hydrogen-Assisted Cracking,” *Metall. Trans. A*, vol. 7, no. 7, pp. 953–960, Jul. 1976.
- [82] Y. Weng, *Ultra-Fine Grained Steels*. Springer Berlin, Heidelberg, 2009.
- [83] H. Fuchigami, H. Minami, and M. Nagumo, “Effect of grain size on the susceptibility of martensitic steel to hydrogen-related failure,” *Philos. Mag. Lett.*, vol. 86, no. 1, pp. 21–29, Jan. 2006.
- [84] A. Shibata, T. Matsuoka, and N. Tsuji, “Effect of Prior Austenite Grain Size on Hydrogen Embrittlement Behaviors in 8Ni-0.1C Steel,” in *Proceedings of the 8th Pacific Rim International Congress on Advanced Materials and Processing*, Springer, Cham, 2013, pp. 583–589.
- [85] R. Padmanabhan and W. E. Wood, “Hydrogen induced cracking in a low alloy steel,” *Metall. Trans. A*, vol. 14, no. 11, pp. 2347–2356, Nov. 1983.
- [86] A. Nagao, K. Hayashi, K. Oi, and S. Mitao, “Effect of Uniform Distribution of Fine Cementite on Hydrogen Embrittlement of Low Carbon Martensitic

- Steel Plates,” *ISIJ Int.*, vol. 52, no. 2, pp. 213–221, Feb. 2012.
- [87] L. Chen, S. Antonov, Y. Su, and L. Qiao, “Dislocation cell walls with high dislocation density as effective hydrogen traps in Armco iron,” *Mater. Corros.*, vol. 73, no. 3, pp. 346–357, Mar. 2022.
- [88] S. J. Kim, D. W. Yun, H. G. Jung, and K. Y. Kim, “Determination of Hydrogen Diffusion Parameters of Ferritic Steel from Electrochemical Permeation Measurement under Tensile Loads,” *J. Electrochem. Soc.*, vol. 161, no. 12, pp. E173–E181, Sep. 2014.
- [89] S. J. Kim and K. Y. Kim, “An Overview on Hydrogen Uptake, Diffusion and Transport Behavior of Ferritic Steel, and Its Susceptibility to Hydrogen Degradation,” *Corros. Sci. Technol.*, vol. 16, no. 4, pp. 209–225, Aug. 2017.
- [90] A. J. Kumnick and H. H. Johnson, “Hydrogen transport through annealed and deformed armco iron,” *Metall. Mater. Trans. B*, vol. 5, no. 5, pp. 1199–1206, May 1974.

Original publications

- I Latypova, R., Kauppi, T., Mehtonen, S., Hänninen, H., Porter, D., & Kömi, J. (2019). Novel stress corrosion testing method for high-strength steels. *Materials and Corrosion*, *70*(3), 521–528. doi:10.1002/maco.201810462
- II Latypova, R., Nyo, T. T., Kauppi, T., Pallaspuuro, S., Mehtonen, S., Hänninen, H., & Kömi, J. (2020). Hydrogen-induced stress corrosion cracking studied by the novel tuning-fork test method. *Materials and Corrosion*, *71*(10), 1629–1636. doi:10.1002/maco.202011767
- III Latypova, R., Seppälä, O., Nyo, T. T., Kauppi, T., Pallaspuuro, S., Mehtonen, S., Hänninen, H., Kömi, J. (2020). Hydrogen-induced cracking of 500 HBW steels studied using a novel tuning-fork test with integrated loadcell system. *Corrosion*, *76*(10), 954–966. doi:10.5006/3592
- IV Latypova, R., Seppälä, O., Nyo, T. T., Kauppi, T., Mehtonen, S., Hänninen, H., Kömi, J., Pallaspuuro, S., Influence of prior austenite grain structure on hydrogen-induced fracture of as-quenched martensitic steels, submitted manuscript.

Reprinted with permission from John Wiley & Sons (Publication I © 2018 WILEY-VCH Verlag GmbH & Co. KGaA, Weinheim), National Association of Corrosion Engineers (Publication III © 2020 AMPP GLOBAL CENTER, INC) and under CC BY 4.0¹ (Publication II © 2020 Authors).

Original publications are not included in the electronic version of the dissertation.

¹ <https://creativecommons.org/licenses/by/4.0/>

839. Rajaniemi, Kyösti (2022) Electrocoagulation in water treatment : continuous versus batch processes and sludge utilization
840. Ramezanipour, Iran (2022) Hybrid spectrum mechanism for energy vertical
841. Saukko, Laura (2022) Managing integration capabilities in collaborative inter-organizational projects
842. Tiensuu, Henna (2022) Modelling the quality of the steel products under challenging measurement conditions
843. Avsievich, Tatiana (2022) Red blood cells and novel nanomaterials : towards nanosafety and nanomedicine
844. Wu, Xiaoting (2022) Machine learning for audio-visual kinship verification
845. Pérez Centeno, Víctor (2022) Merging neuroscience technologies in entrepreneurship research
846. Cajander, Niko (2022) Temporary agency work and worker well-being at restaurants : insights into socially sustainable work
847. Nouri, Parisa (2022) Cooperative diversity mechanisms for critical machine-type communications
848. Afonin, Nikita (2022) Development of passive seismic interferometry to study shallow subsurface structure
849. Sdobnov, Anton (2022) Laser speckle contrast imaging for functional visualization
850. Tampio, Kari-Pekka (2022) Enhancing value creation at the front-end of a collaborative hospital construction project
851. Annunen, Petteri (2022) Industrialization in construction : a process model for capability creation
852. Omodara, Linda (2022) Developing and testing sustainability assessment tools for chemical processes and products : case study on critical rare earth elements
853. Karimidastenaeei, Zahra (2022) The potential of unconventional water in limiting water scarcity
854. Kallio, Rita (2022) Multidisciplinary study of the beneficiation potential of the Kiviniemi ferrous scandium deposit
855. Kiani, Sepideh (2022) Development of passive bioreactors treating different types of low carbon wastewater in cold climate conditions

S E R I E S E D I T O R S

A
SCIENTIAE RERUM NATURALIUM
University Lecturer Tuomo Glumoff

B
HUMANIORA
University Lecturer Santeri Palviainen

C
TECHNICA
Postdoctoral researcher Jani Peräntie

D
MEDICA
University Lecturer Anne Tuomisto

E
SCIENTIAE RERUM SOCIALIUM
University Lecturer Veli-Matti Ulvinen

E
SCRIPTA ACADEMICA
Planning Director Pertti Tikkanen

G
OECONOMICA
Professor Jari Juga

H
ARCHITECTONICA
Associate Professor (tenure) Anu Soikkeli

EDITOR IN CHIEF
University Lecturer Santeri Palviainen

PUBLICATIONS EDITOR
Publications Editor Kirsti Nurkkala

ISBN 978-952-62-3509-7 (Paperback)
ISBN 978-952-62-3510-3 (PDF)
ISSN 0355-3213 (Print)
ISSN 1796-2226 (Online)